Photochemical & Photobiological Sciences

ROYAL SOCIETY OF CHEMISTRY

PAPER

View Article Online
View Journal

Cite this: DOI: 10.1039/d0pp00145g

In flow metal-enhanced fluorescence for biolabelling and biodetection

Daniela Gontero,[a] Alicia V. Veglia [b] and A. Guillermo Bracamonte *[b,c]

Escherichia coli bacteria were determined by in flow cytometry with laser excitation and fluorescence detection applying ultraluminescent core–shell nanoparticles based on Metal Enhanced Fluorescence (MEF). Core–shell nanoparticles consisted of a 40 nm core modified with a silica spacer grafted with Rhodamine B (RhB). The electromagnetic field in the near field of the core surface enhanced the fluorescence of RhB by plasmonic and fluorophore coupling. The hydrophilic silica spacer allowed the non-covalent interaction with the polar *E. coli* surface and thus ultraluminescent bacteria biolabelling was developed. Clearly, well defined and bright bacteria imaging was recorded by Laser Fluorescence Microscopy based on the non-covalent deposition of the ultraluminescent nano-emitters. Using these nano-labellers, it was possible to detect labelled *E. coli* by in flow cytometry. Higher values of Side-scattered light (SSC) and Forward-scattered light (FSC), and number of fluorescent event detections, were observed for labelled bacteria compared to those non-labelled. The sensitivity of the methodology was evaluated by varying bacteria concentration and acceptable analytical figures of merit were determined. Applying this methodology we could quantify *E. coli* from a synthetic real sample of fortified water. Similar results were obtained by bacteria counting with Laser Fluorescence Microscopy and with a cell-bacteria counter.

Received 14th April 2020,
Accepted 13th July 2020

DOI: 10.1039/d0pp00145g

rsc.li/pps

1. Introduction

In flow cytometry is a versatile technique that could be applied to pathogen detection within clinical chemistry, biochemistry, medical diagnosis,[1] environmental samples[2] and genetic studies.[3] For all these applications new tools should be developed in order to increase signal and improve detection.[4] Different approaches were developed depending on the optical detection technique applied, such as light scattering,[5] absorption and photoacoustics.[6] However, fluorescence detection is highly sensitive and thus allows obtaining further information from in flow imaging cytometry instrumentation.

For these reasons fluorescent probes,[7] fluorescent probes *in vivo*,[8] fluorophores bioconjugated with antibodies,[9] fluorescent proteins,[10] fluorescent polymers,[11] quantum dots[12] applied to biolabelling and cytometry applications are of particularly considerable interest. Yet, enhanced signals are still pose a challenge and new detection techniques were applied as Surfaced Enhanced Raman Scattering (SERS).[13]

Thus, we are interested in developments of in flow methodologies coupled to fluorescence detection and NanoImaging applied for genotyping with high impact on advanced ultrasensitive diagnostics and personalized nanomedicine. For example/instance, D. Boudreau *et al.* developed a high-throughput method in flow single particle detection of core–shell biosensor for genotyping based on capillary tubing with fibre-coupled diode laser and camera.[14] In addition, due to the interest in the development of new in flow optical set-ups and instrumentation, a patent on Patterned Capillary Device and its productions process was reported.[15]

Then, the synthesis of ultraluminescent gold core–shell nanoparticles applied to individual bacterial detection based on Metal-Enhanced Fluorescence (MEF) NanoImaging was reported by Bracamonte *et al.* with potential application in imaging cytometry for clinical diagnosis. Their ultraluminescent properties could be tuned by optimizing their metallic cores, nanoparticle size, shape and plasmonic properties in order to obtain optimal enhancement.[16] Moreover, these enhanced nano-emitters were versatile, biocompatible and chemically modifiable surfaces that enabled single *E. coli* detection by Laser Fluorescence Microscopy.[17]

The MEF phenomenon from core–shell nanoarchitectures[18] could be attributed to different radiative pathways from the

[a]*Laboratorio de Análisis Clínicos y Bacteriológicos, Clínica de la Familia II, Río Tercero, 5850 Córdoba, Argentina*
[b]*Instituto de Investigaciones en Físico Química de Córdoba (INFIQC), Departamento de Química Orgánica, Facultad de Ciencias Químicas, Universidad Nacional de Córdoba, Ciudad Universitaria, 5000 Córdoba, Argentina.*
E-mail: gbracamonte@fcq.unc.edu.ar, guillermobrac@yahoo.ca
[c]*Departement de chimie and Centre d'optique, photonique et laser (COPL), Université Laval, Québec, QC, Canada, G1V 0A6*

interaction of a fluorophore placed at accurate distances[19,20] from a high intensity electromagnetic field generated by electronic oscillation on surfaces of metallic core with laser excitation.[21,22]

In flow methodologies showed to be faster and cheaper for the development of new bioanalytical methodologies. In addition, the incorporation of ultraluminescence properties from the nano-scale for in flow enhanced fluorescence event detections and counting has drawn special attention. To the best of our knowledge, in flow MEF combined with standard in flow methodologies such as in flow cytometry has not yet been reported. Hence, in order to incorporate the use of ultraluminescent gold core–shell nanoparticles as nano-labellers for enhanced biodetection, the present research shows the application of ultraluminescent gold core–shell nanoparticles for *E. coli* labelling and detection by in flow cytometry with laser excitation and fluorescence detection.

2. Experimental

2.1 Apparatus

The flow cytometer was purchased from BD Company. The model used was FACSCanto II analyzer (BD Biosciences). The data was analyzed with FlowJo V10 software (TreesStar) and FacsDiva software. Laser excitation at 488.0 nm and 555.0 nm with standard filters at 533/30 and 585/40 for Alexa Fluor 488-A and AF5555-A were applied. OLYMPUS Confocal Laser Scanning, FV1000, FLUOVIEW, was used for fluorescence microscopy images. Bacteria counter BD BACTEC™ FX was purchased from BD Company. Shaker with oscillation mode and Vortex for Bacteria labelling was provided by Thermo-Fischer Scientific Company. Transmission electron microscopy (TEM) images were taken using a TEM JEM-1230, JEOL, with an operating voltage of 200 kV.

UV-vis and spectrofluorimetric determinations were carried out in a Varian UV-50 Carry 50 Conc. and a Cary-Eclipse, respectively. An ultrasonic bath (Branson 2510) was used for the solubilisation and dispersion of the reagents, and colloidal dispersions, respectively. Centrifugations were done using the Eppendorf Centrifuge 5804 (rpm range 7500–8000 rpm). Data analysis was performed with origin (Scientific Graph system) version 8.

2.2 Reagents

The biostructures evaluated were *E. coli* as Gram negative bacteria purchased from Sigma-Aldrich. The components of culture medium for bacteria growth used in growing and maintaining bacterial cultures were supplied by the same company. For in flow cytometry, micro-meter multicolor beads purchased from BD Company were used as control. Water was obtained using a Millipore apparatus. RhB (99% purity, Sigma-Aldrich), hydrogen tetrachloroaurate, $HAuCl_4{\cdot}3H_2O$ (99%, Sigma-Aldrich), citrate sodium tribasic dehydrate (99%, ACS reagent), TEOS Tetraethyl orthosilicate (98%, Sigma-Aldrich), Ethanol (Sintorgan, HPLC grade), 3-(aminopropyl)triethoxysilane, APS (98%, Sigma-Aldrich), *N*-hydroxysuccinimide (NHS) and *N*-(3-Dimethylaminopropyl)-*N*′-ethylcarbodiimide hydrochloride (EDC) (98%, Sigma-Aldrich) and sodium cyanide (95%, Sigma-Aldrich) were used.

2.3 General procedure

The procedures were optimized from our previous synthesis of core–shell nanoparticles and nanocomposites already published from our laboratory. The fluorescence emission was optimized by adjusting the incorporation of optimal fluorescence reporter concentrations for maximal enhancements.[16] These nanostructures were applied for *E. coli* bacterial biolabelling.[17]

Gold nanoparticles were synthesized by the classical Turkevich method of citrate reduction of $HAuCl_4$ and afterward stabilized with PVP 40. The nanoparticle diameter tuning was obtained by being modified the ratios of $HAuCl_4$/Citrate to smaller values. Molar ratio applied = 1.0; for 40 nm. The resulting nanoparticles were then redispersed in anhydrous ethanol (mother solution, [Au NPs] = 3.88×10^{10} NPs per mL, for 40 nm diameter). Core–shell nanoparticles were synthesized by a modified Störber method.[23] For a typical synthesis of gold core–shell nanoparticles (Au@SiO_2) with silica shell spacer length of 7–9 nm, 7.5 μL volumes of TEOS 10.0% in ethanol in a basic (pH = 8–9) with NH_4OH (Scheme 1a (i) and (ii)) was added to 4 ml of 40 nm gold nanoparticles PVP stabilized with vigorous agitation. The reaction time was 15 h (Scheme 1a). These nanostructures were used as chemical platforms in order to functionalize their surfaces with luminescent properties by RhB fluorescent dye (Scheme 1a (iii)). The RhB was incorporated by covalent bonding with APS by NHS/EDC activation in order to yield RhB-APS conjugated. Then for RhB linking over the silica surface, from this solution increasing variable volumes of RHB-APS were added to 1 ml of Au@SiO_2 with continuous stirring. The reaction time was 20 min; immediately after a second thin silica shell was added with a solution of TEOS 2.5% for core–shell nanoparticles (Scheme 1a (iv)). The reaction was then left to react 24 h. At each step of the synthesis the nanoparticles were centrifuged and redispersed in anhydrous ethanol.

The ultraluminescence properties were controlled by digestion of the gold cores with the Sodium Cyanide leakage method.[24] Vortex overnight of the samples was applied in the presence of 0.5 μM of Sodium Cyanide. Thus, core-less nanoarchitectures ((–)@SiO_2-RhB) were synthesized. The Metal-Enhanced Fluorescence Enhancement Factor (MEF_{EF}) was determined from the ratio of emissions of Au@SiO_2-RhB and (–)@SiO_2-RhB nanostructures. Optimal samples with MEF_{EF} values within 9–10 interval were used for nano-biolabelling assays.

In order to quantify the RhB incorporated into the silica, two methods were used: one based on the supernatant collection of each sample after the centrifugation step of the reaction with APS-RHB; the other was based on the liberation of the RhB from the silica spacer from core-less nanoarchitectures obtained with a high-speed centrifugation in a strong

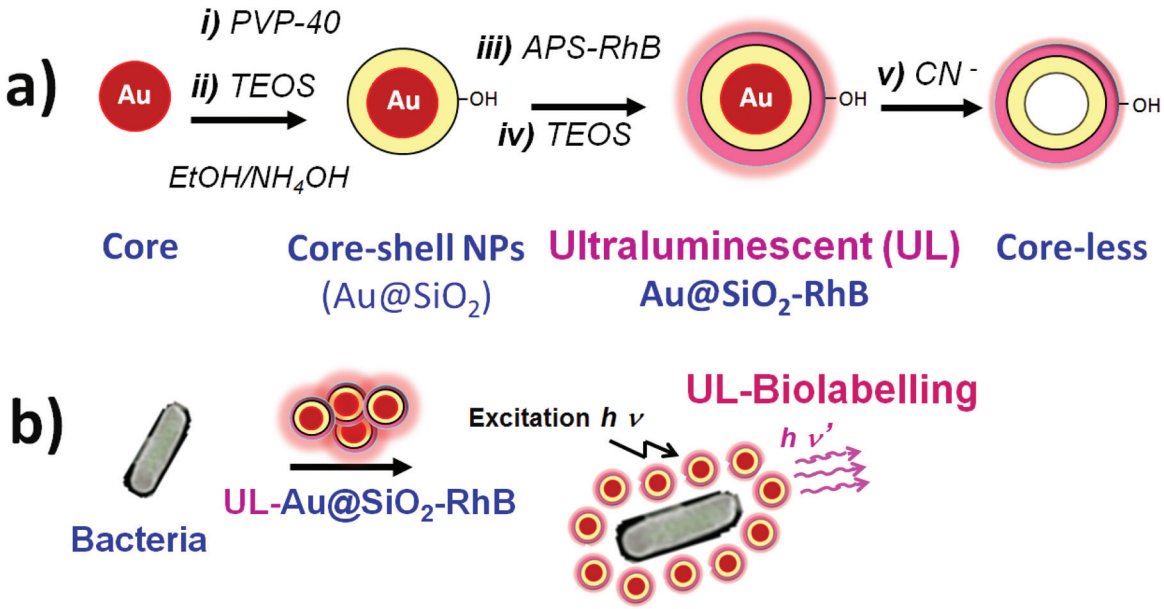

Scheme 1 (a) Synthesis steps of ultraluminescent gold core–shell nanoparticles (Au@SiO_2-RhB): gold cores stabilization with polyvinyl-pyrrolidone (PVP) (i); silica shell by TEOS tetraethyl orthosilicate added to basic media (ii); Rhodamine B (RhB) conjugated with 3-(aminopropyl)triethoxysilane (APS) (APS-RhB) (iii); second thinner silica shell with TEOS (iv); synthesis of core-less nanoparticles by sodium cyanide addition (v). (b) Scheme of Bio-ultraluminescent labelling of *E. coli* by addition of ultraluminescent core–shell nanoparticles based on Metal Enhanced Fluorescence (MEF).

acid media (pH = 1–2). Then, from a calibration curve with APS-RhB, the concentration of RhB covalently bonded to the silica shell was estimated (mean concentration values were calculated from 3 different synthesis batches).

For bacteria-nanoparticle interaction, a dispersion of bacteria prepared from concentrated bacteria dispersion was done. Growth rates and bacterial concentrations were determined by measuring optical density (OD) at 600 nm each 30 min (OD of 0.1–0.2 corresponds to concentrated conditions of 10^8 cells per mL) based on the McFarland methodology.[25] The bacteria for bacteria dispersion preparation came from the culture growth media. Moreover, the different samples of the colloidal dispersions of *E. coli* were counted by the classical cell counting methodology using standard designed chambers on glass slides coupled to Confocal Microscopy.[26] Bright Field Microscopy and Laser Fluorescence Microscopy techniques were coupled.

For bacterial fluorescent labelling, the dispersions prepared were in contact with ultraluminescent Au@SiO_2-RhB nanoparticles from 0.9 to 5×10^8 NPs per mL for 24 h (Scheme 1b). Therefore, deposed 40 nm Au@SiO_2-RhB nanoparticles over *E. coli* bacteria with Ultraluminescent properties (UL-Biolabelling) were obtained. The improved methodology was based on a previous one that we developed.[17] The deposition of the Au@SiO_2-RhB nanoparticles on *E. coli* was based on non-covalent interactions between the silanized nanosurfaces and the polar membrane constituents.[27,28]

The work-flow used for all the in flow cytometry experiments of labelled *E. coli* was: (a) nano-biolabelling of *E. coli*; (b) nano-biolabelling checking by Laser Fluorescence Microscopy; and (c) detection and quantification by in flow cytometry. For quantification, the sensitivity of the Cytometer was verified by preparing at least one point of the calibration curve.

For in flow cytometry experiments, dilutions for the calibration curve were prepared from the concentrated dispersion with variable additions within the interval of volumes of (10–250) μL into 2 mL as a final volume. Water from a Millipore apparatus was used to prepare all the colloidal dispersions, whereas tap-water from the University was used for the synthetic real water sample fortification with *E. coli*. Water filtration were carried out by HPLC filter with porous size of 0.25 μm.

For the Limit of Bacteria Detection (LBD) concentrations of the initial *E. coli* in concentrated conditions in colloidal dispersion were decreased to a lower level of concentration. Hence, additions of μL aliquots were made from a dilution of $1/1 \times 10^5$ times prepared from the initial concentrated bacteria colloidal dispersion. For example, for a typical experiment within low concentrations, 5 μL were added to 50 μL and higher volumes within 1 ml total volume.

3. Results and discussion

3.1 Characterization of luminescence properties of gold core–shell nanoparticles

Gold core–shell nanoparticles were synthesized from the modification of 40.0 nm gold core templates with variable silica shell lengths for tuning of luminescence properties. The gold core-templates (Au) were obtained by the Turkevich method[29] by the reduction reaction of hydrogen tetrachloroaurate

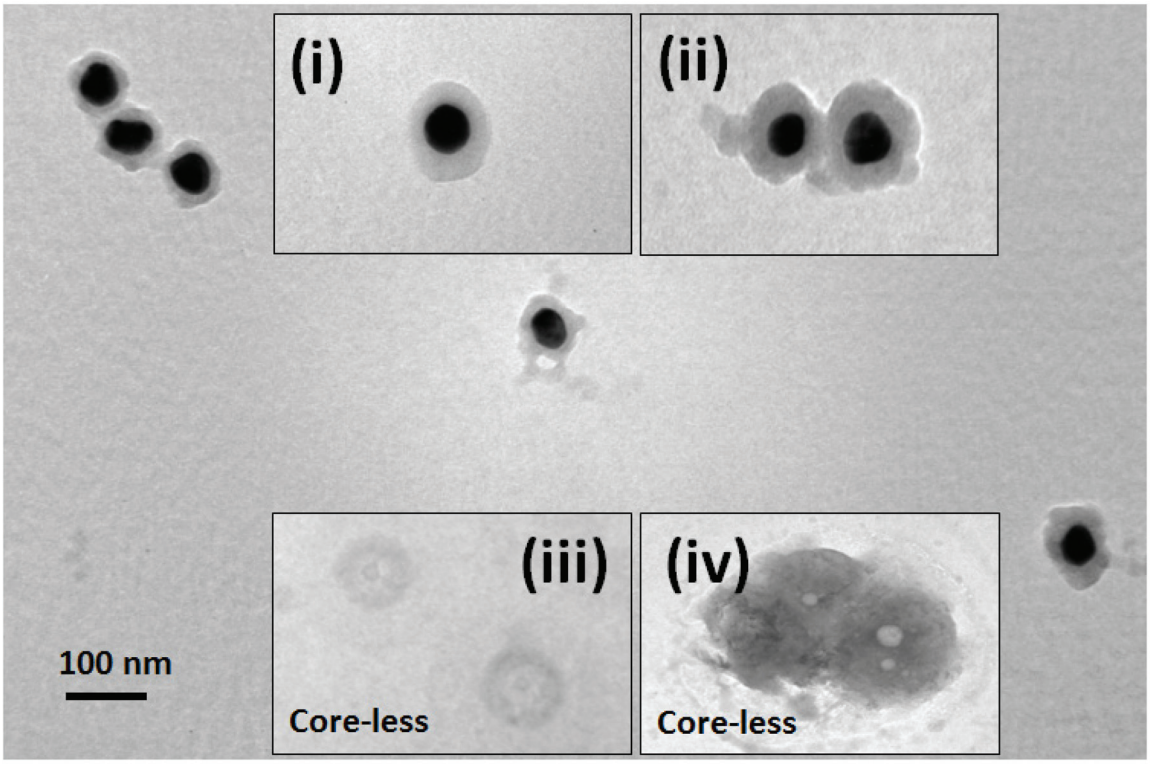

Fig. 1 TEM images of core–shell nanoparticles, Au@SiO_2, synthesized by the Störber method with optimized silica spacer length for enhanced fluorescence emissions. Inset images: (i) 9–11 nm; (ii) 20 nm; (iii) core-less nanoparticles of 9–10 nm; (iv) aggregated core-less nanostructures.

($HAuCl_4$) with citrate. The size of the spherical nanostructures was adjusted by controlling the ratio of $HAuCl_4$/citrate concentrations.[17] Then, by applying a modified Störber methodology recently developed by us for MEF applications,[16] gold core–shell silica nanoparticles (Au@SiO_2) were prepared (Fig. 1). The silica spacer lengths (@SiO_2) were varied from 2 to 25 nm and greater lengths to place modified fluorescent silica layer with Rhodamine B (RhB). Therefore, different and controlled fluorescent shells were deposed over gold core–shell nanoparticles with variable distances from the gold surfaces (Au@SiO_2-RhB). The silica shell formation showed to be highly dependent on the hydroxide concentration from the ammonium hydroxide addition due to the nucleophilic substitution mechanism involved. Moreover the surface passivation within ethanol showed to be an important factor to control. This was explained on the basis of more affinity of TEOS monomers on the PVP-40 molecules adsorbed on well dispersed gold nanoparticles than with the surrounding media, not observed with citrate. Hence controlling the passivation agent, the concentration of hydroxide and the media templated controlled polymerization[30] was formed on nanoparticles.[31] Therefore, by varying TEOS concentrations, variable silica spacer shells (@SiO_2) were prepared. The control of the silica shell lengths was done by TEM. Homogeneous silica shells were obtained within 7–10 nm lengths (inset image (i) of Fig. 1); while longer shells such as 20–25 nm led to bigger nanoparticles that formed from dimmers to higher nanoaggregates patterns (inset image (ii) of Fig. 1).

This fact was explained by the available concentration of the organosilane, Tetraethyl orthosilicate (TEOS). In presence of lower concentration it was homogeneously deposed the silica shells around the gold templates; while at higher concentrations the deposition and growth arrived to contact adjacent gold core–shell nanoparticles in progress of formation.

Regarding the recorded emissions from the Au@SiO_2-RhB nanoplatforms, variable emissions were recorded according to the silica spacer lengths. High Luminescent Au@SiO_2-RhB nanoparticles were recorded by Laser Fluorescence Microscopy accompanied with completely diminished photobleaching properties.

The diminished photobleaching properties and enhanced emissions were generated from the fluorophores incorporated in the modified silica shell only in the presence of the gold cores within the optimal high energy electromagnetic field within the near field. This was attributed to the MEF phenomenon as described in previous research.[16,17,32–37] The concentration of RhB incorporated into the silica shell obtained was 0.057 μM. This value was slightly lower than that obtained from the original previous nanoparticles obtained by us (0.075–0.093 μM), which allowed decreasing a small fraction of RhB quenched and obtaining brighter nanoparticles from well resolved nanostructures.

Optimal emissions were recorded from silica spacer shells of 8–10 nm generating the well-defined Luminescent dots with high emission intensities. These nanoarchitectures showed variable ultraluminescent nanoaggregate formation (Fig. 2a) in

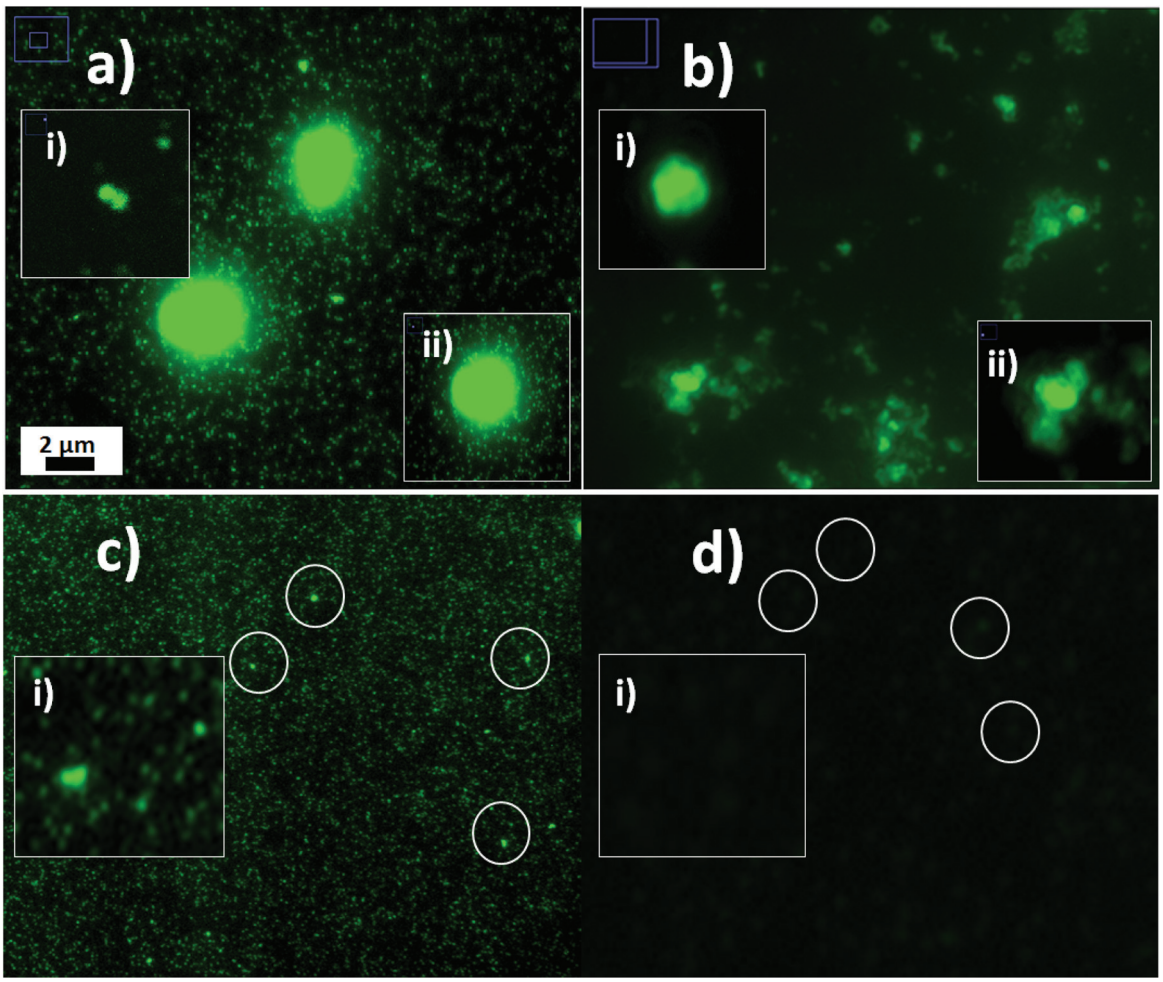

Fig. 2 Fluorescent microscopy of ultraluminescent 40 nm core–shell nanoparticles Au@SiO_2-RhB: (a) higher nano-aggregates of Au@SiO_2-RhB, with optimal silica spacer of 9–10 nm. Inset image: (i) dimmer resolution, (ii) higher nanoaggregates; (b) Au@SiO_2-RhB, silica spacer 15 nm. Inset image: (i) tetrameter resolution, (ii) nanoaggregates; (c) well-dispersed optimal ultraluminescent Au@SiO_2-RhB nanoparticles for biolabelling. Inset image: (i) single nanoparticle resolution; (d) core-less nanoparticles, (–)@SiO_2-RhB, obtained by addition of sodium cyanide. [NPs] = 4–5 × 10^{10}; [RhB] = 0.057 μM.

colloidal dispersion according to their concentration. At lower nanoparticle concentrations (dilutions 1/100 from the concentrated batch of synthesis), individual dot sizes were correlated with single Au@SiO_2-RhB nanoparticles below the diffraction limit[38,39] (inset (i) of Fig. 2). At concentrated nanoparticle conditions (concentration directly obtained from the condition of the synthesis developed), the presence of nanoaggregates (inset (ii) of Fig. 2) was recorded. It should be highlighted that the optimized ultraluminescent properties were observed in diluted as well concentrated conditions. It should also be mentioned that these ultraluminescent higher size nano-aggregates of Au@SiO_2-RhB were easily redispersed by a few seconds of sonication. And this size of aggregation was obtained only in concentrated conditions. This fast redispersibility showed high stability of the nanoparticles within the colloidal dispersion. However, in concentrated conditions, due to the proximity of small nanosizes related to optimal ratio of van der Waals forces and nanosurfaces. This ratio was reported to exponentially increase close to 40 nm gold nanoparticles by the Hamaker constants.[40,41]

In the presence of longer silica spacer lengths of 20–25 nm, their emissions were drastically decreased (Fig. 2b). The higher size gold core–shell nanoparticles generated bigger nanoparticle aggregates (inset (i) of Fig. 2b) with lower resolution in comparison with well resolved single nanoparticles and dimeric species from shorter silica shell length observed (inset (i) of Fig. 2a). Yet, bigger luminescent Au@SiO_2-RhB nanoplatforms (inset (ii) of Fig. 2b) were observed with lower frequency.

Accordingly, by controlling the silica spacer length and concentration of ultraluminescent gold core–shell nanoparticles, well dispersible ultraluminescent nanoparticles detection was achieved within colloidal dispersions (Fig. 2c), from where ultraluminescent dots were recorded below the diffraction limit of 90–100 nm (inset Fig. 2c). Thus, unless 25–30% of size increase was generated by the generation of non-classical light by MEF with Laser Fluorescence Microscopy, considering

70 nm as the optimal size for Au@SiO_2-RhB nanoparticles recorded by TEM.

Then, in order to evaluate the MEF_{EF}, core-less nanoparticles were formed by the Sodium Cyanide methodology.[16,24] In this way, increased photobleaching properties were developed, generating lower emissions from core-less nanoarchitectures than from core–shell nanoparticles (Fig. 2d). The formation of core-less nanostructures was verified/confirmed by TEM microscopy (inset (iii) and (iv) of Fig. 1). The core-less nanoarchitectures showed less contrasted cores in the absence of the gold nano-template due to their digestion by addition of Sodium Cyanide.

From the ratio of emission intensities (Int.) from single and dimeric Au@SiO_2-RhB, and (–)@SiO_2-RhB nanostructures, MEF Enhancement Factors (MEF_{EF} = Int. Au@SiO_2-RhB/Int. (–)@SiO_2-RhB) were determined. The emissions were recorded from Laser Fluorescence Microscopy NanoImaging. Therefore, maximal MEF_{EF} values of 36 and 39 were determined for single nanoparticles and dimeric species, respectively, with optimized 9–10 nm silica spacer shells. These values were similar as those previously determined from optimized gold core–shell nanoparticles applied to single *E. coli* detection by Laser Fluorescence Microscopy.[17] However, it should be noted that in the present research the resolution of single nanoparticle detection and control of their aggregation based on the control of their concentration was optimized. Thus, improved biolabelling was expected for better/a more efficient in flow nano-biostructure detection and counting. This was also supported by the increased dispersibility of nano-biostructures as compared to non-labelled biostructures.

Finally, in order to determine the stability of the colloidal dispersion of the optimal samples with ultraluminescent properties with the higher MEF_{EF}, their concentrations were varied. Therefore, a decrease was observed in the detection frequency of higher nanoaggregates, in addition to an increase in smaller ones and in the size of bright dots close to single nanoparticles. Moreover, higher contrast images were recorded due to the decrease in luminescence from the deeper background caused by the presence of less nano-emitters. Therefore, we recorded, in optimal lower concentration conditions, Single Au@SiO_2-RhB nanoparticles to tetramers (Fig. 3) and smaller nano-aggregates than 600 nm (inset (i) of Fig. 3). It should be noted that this stability and capability/capacity of interaction for attraction and dispersion were also shown by Dynamic Light Scattering (DLS) measurements. Well-shaped Gaussians size distributions were detected during unless 10 min.

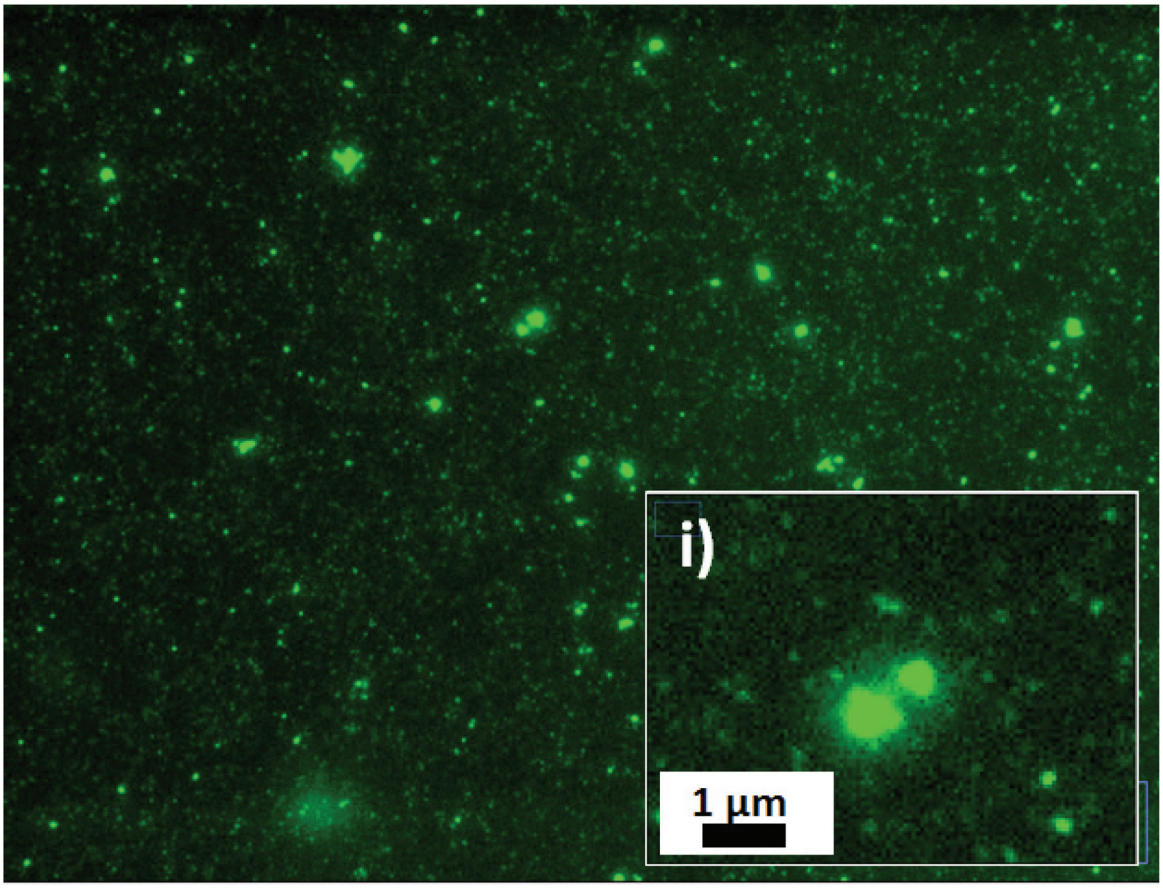

Fig. 3 Fluorescent microscopy of ultraluminescent 40 nm core–shell nanoparticles Au@SiO_2-RhB in shorter concentration intervals. [NPs] = 1–2 × 10^8; [RhB] = 0.057 μM.

Thus, homogeneous 40 nm gold core–shell nanoparticles were prepared with ultraluminescent properties and decreased photobleaching properties that showed well dispersible characteristics based on their polar silanized surfaces for biomembrane interactions. These optimized Au@SiO_2-RhB nanoparticles were used as nanolabellers for *E. coli*.

3.2 In flow evaluation of ultraluminescent gold core–shell nanoparticles detection by cytometry for biolabelling applications

For in flow applications optimal enhanced luminescent Au@SiO_2-RhB nanoparticles were evaluated by in flow cytometry. By analysis of contour plots of side-scattered light (SSC) *vs*. forward-scattered light (FSC), different detection distributions of the nano-emitters were observed (Fig. 4). It should be mentioned that the FSC is proportional to the structure or cell-surface area or size, while the SSC is proportional to structure or cell granularity or internal complexity.[42,43] Thus, the correlation of FSC and SSC values related to their nanoparticle aggregation and scattered light properties was recorded. In this way, in the optimized ultraluminescent nanoparticles sample, the FSC distribution value was centered at $\times 10^4$ with a large SSC distribution within $\times 10^1$–10^4 interval of values (Fig. 4a). Hence, a varied correlation of SSC and FSC values was found for the different sizes of nanoparticles corresponding to different nanoaggregate sizes within the colloidal dispersion.

The intervals of values of FSC and SSC for the Au@SiO_2-RhB nanoparticles corresponded to different nanoaggregate size distributions that generated varied scattered light patterns. The upper distribution of both parameters highlighted in blue shows the variable fluorescent event detection counting (Fig. 4a) that correlates with their emission properties recorded by fluorescence depending on the silica spacer lengths incorporated into the Au@SiO_2-RhB nanoplatforms.

The fluorescent event detection counting clearly/markedly differed from the samples by analysis of Alexa Fluor 488-A *vs.* AF555-A Plots (Fig. 4b). These nominated Alexa Fluor 488-A and AF555-A standard variables were generated from data recording based on fluorescence event detection by laser excitations at 488.0 nm and 555.0 nm with emission filters placed at 530/30 nm and 585/42 nm, respectively.

Therefore, the distributions of fluorescent event detection counting were assigned as D1 with blue and D2 with violet for 488.0 nm and 555.0 nm laser excitation, respectively (Fig. 3b). The detection and counting of the Au@SiO_2-RhB were clearly shown with Alexa Fluor 488-A *vs.* AF555-A Plots collected from the upper region of the SSC *vs*. FSC graphs. Thus, higher fluorescent event counting was recorded by 555.0 nm laser excitation rather than by 488.0 nm. This was/is attributed to the better excitation of the RhB fluorophore and gold Core Plasmon coupling centered at 540.0 nm for the size of this gold core template and nanoarchitecture.

Moreover, a higher number of fluorescent event detection counting were collected from optimized ultraluminescent Au@SiO_2-RhB with Silica spacer ranging 8–11 nm. These optimized nanoemitters showed maximal emissions based on MEF as compared to nanoarchitectures with longer silica spacer, with decreased MEF emissions and increased photobleaching properties ((–)@SiO_2-length = 20 nm and 25 nm).

Thus, the tendency was correlated with results yielded by Static Fluorescence and Laser Fluorescence Microscopy and explained by MEF. The detection of non-classical light generation from fluorescent-modified 40 nm gold core templates by in flow cytometry with laser excitation allowed the detection of individual fluorescent events within colloidal dispersion. Here, we considered the effective laser beam surface of impact (square ≅500 × 500 nm) for detection, in addition to the targeted sizes (below and beyond of ≅100 nm depending on the nanoaggregation status).

Then to corroborate the effect of the core on the emissions of Au@SiO_2-RhB nanoparticles, we evaluated the detection and counting of the core less (–)@SiO_2-RhB nanostructures. Accordingly, a clear lower number of fluorescent events from (–)@SiO_2-RhB were collected and compared to Au@SiO_2-RhB nanoparticles. From SSC *vs*. FSC graphs, the counting from the upper region was significantly decreased; SSC *vs*. FSC values also decreased from the lower region (lower SSC values and larger FSC value interval) (Fig. 4c). The values found in the upper region of the plots were attributed to absence of the core template with diminished emissions and increased photobleaching properties. The modification in the lower region was attributed to the core-less nanoarchitecture, generating higher aggregates with lowered emissions. Alexa Fluor 488-A *vs*. AF555-A Plots showed a large decrease in the fluorescent event detection counting at both excitation lasers applied (Fig. 4d).

Thus, the detection and counting of subwavelength nanoarchitectures below 100 nm were carried out within in flow cytometry with laser excitation and fluorescence detection. Non-labelled *E. coli* detection by SSC *vs*. FSC distributions and Alexa Fluor 488-A *vs*. AF555-A Plots analysis were then made. These types were characterized as optical transparent bacteria[44,45] contrasting with other types such as Fluorescent Cyanobacteria.[46,47]

From the SSC *vs*. FSC graph, main distribution of detection events was registered within $\times 10^3$–10^4 and $\times 10^4$ for SSC and FSC, respectively (Fig. 5a). This central region was varied from lower values of SSC in relation to bacteria concentrations; however, the upper region linked to the detection of fluorescent events from Au@SiO_2-RhB nanoparticles was not modified. This was corroborated with Alexa Fluor 488-A *vs*. AF555-A plots that showed low fluorescent event detection counting at different bacteria concentrations (Fig. 5b), whereas the lower region related to scattered light was partially overlapped with Au@SiO_2-RhB nanoparticles.

Thus, different distributions of detection events were recorded for *E. coli* and Au@SiO_2-RhB nanoparticles. This showed the potential application for detection of the synthetic nano-biostructures. Thus, in the next step these Au@SiO_2-RhB nanoparticles were studied as nanolabellers for *E. coli* detection.

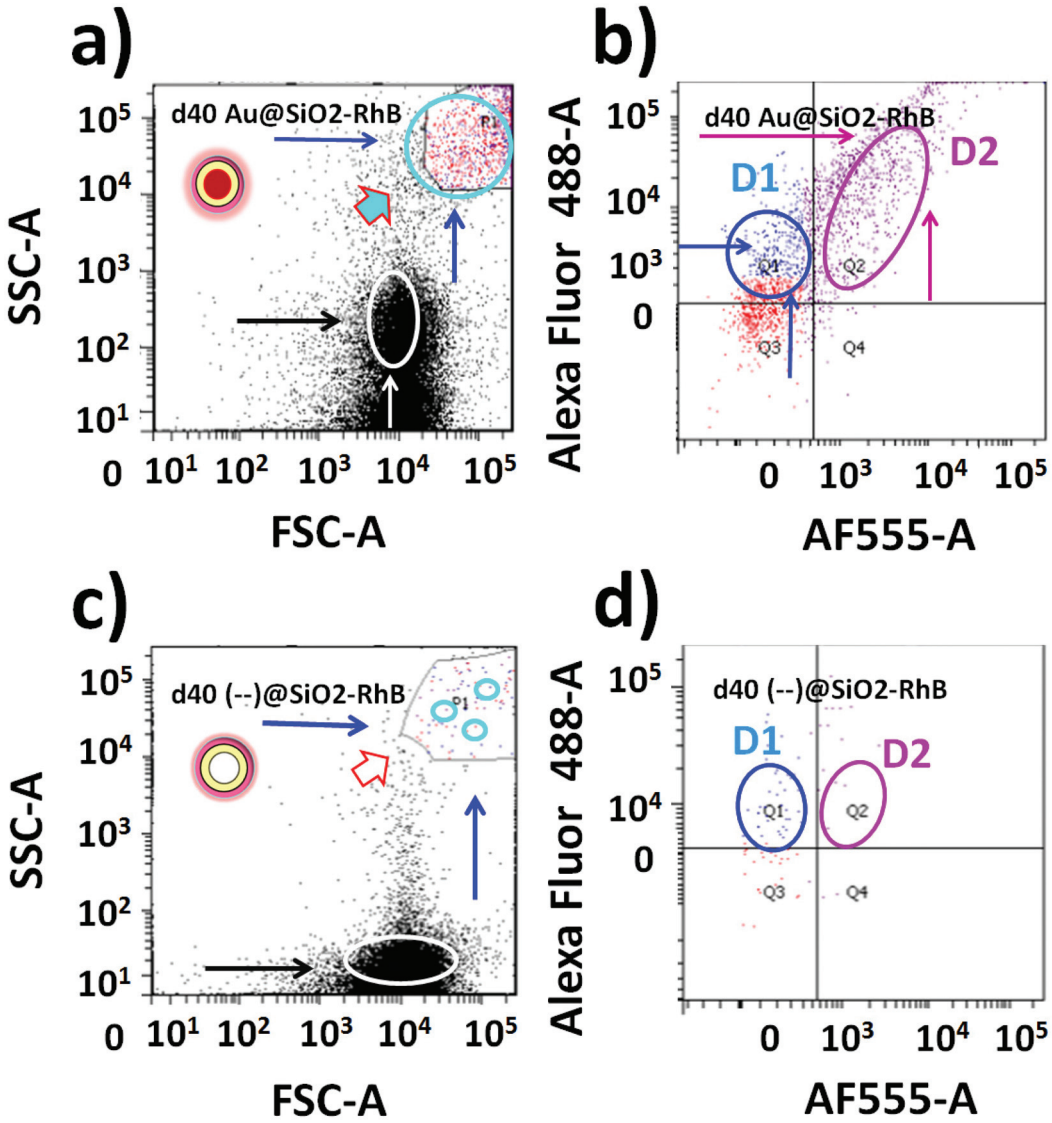

Fig. 4 (a) In flow cytometry of 40 nm gold core–shell nanoplatforms (Au@SiO_2-RhB) with (@SiO_2-) = 12.0 nm. Contour plots of Side-scattered light, SSC (SSC is proportional to cell granularity or internal complexity) *vs*. Forward-scattered light were analyzed, FSC (FSC is proportional to cell-surface area or size); (b) fluorescent event detection counting of Au@SiO_2-RhB by laser excitation at 488.0 nm and 555.0 nm with emission filters at 530/30 nm and 585/42 nm, for Alexa Fluor 488-A *vs*. AF555-A, respectively (D1 = blue distribution recorded with 488.0 nm laser excitation; and D2 = violet distribution with 555.0 nm excitation); (c); and (d) core-less nanoarchitecture detection by in flow cytometry by contour plots of SSC *vs*. FSC; and (d) Alexa Fluor 488-A *vs*. AF555-A graphs.

3.3 Ultraluminescent *E. coli* bio-labelling based metal enhanced fluorescence

The ultraluminescent properties based on 40 nm gold core–shell nanoparticles (Au@SiO_2-RhB) obtained were applied to *E. coli* labelling. By applying the developed methodology of non-covalent deposition over bacteria varied ultraluminescence intensities were observed from individual and aggregated nano-biostructures.

In concentrated *E. coli* conditions, decreased luminescence intensities (see Fig. 6a) were found in comparison to higher ultraluminescent Au@SiO_2-RhB nanoparticles (inset image of Fig. 5a). However, a high degree of correspondence was observed between the labelled bacteria detected by Laser Fluorescence Microscopy and by Bright Field Microscopy. Therefore, the accurate deposition over the biostructures produced well-defined bright labelled biostructures. This synthetic Luminescent property generated faster detections than those from traditional Bright Field Microscopy (Fig. 6b). In diluted conditions, even if the ultraluminescent core–shell nanoparticles showed formation of clear and bright small nanoaggregates (inset Fig. 5a), Enhanced ultraluminescent biostructures were recorded (Fig. 5c). By green LUT edition ("Look Up at Table", image LUT adjustment parameters), a clear improved resolution was obtained from individual bacteria (inset Fig. 6c), as compared to Bright Field Microscopy (inset image of Fig. 6b). Hence, by a complete ultra-

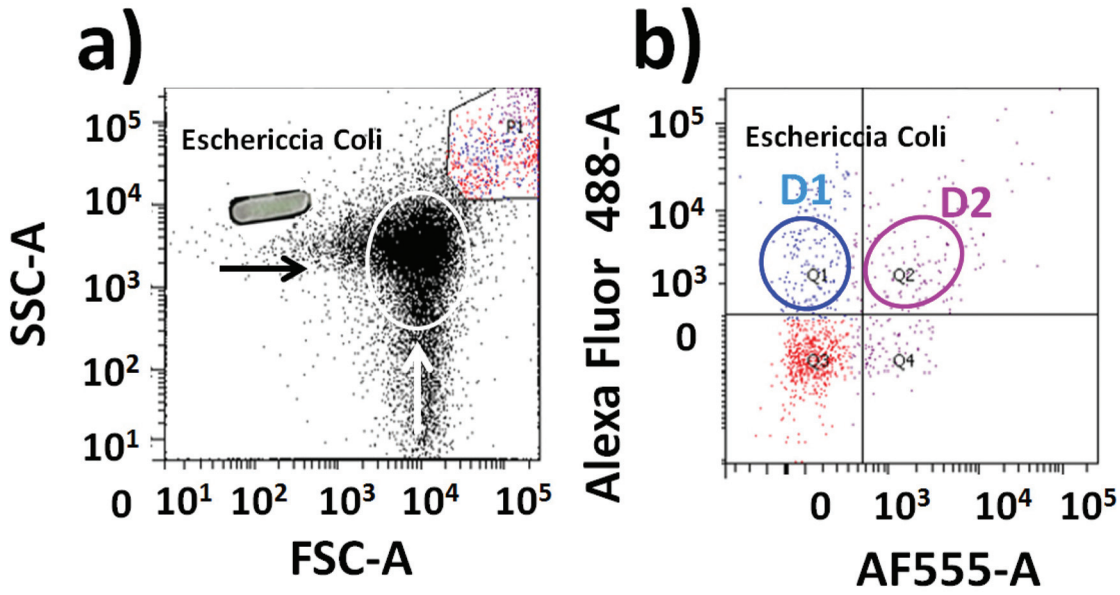

Fig. 5 In flow cytometry of non-labelled *E. coli*: (a) analysis of contour plots of Side-scattered light, SSC (SSC is proportional to cell granularity or internal complexity) *vs.* Forward-scattered light, FSC (FSC is proportional to cell-surface area or size); (b) fluorescence event detection by laser excitation at 488.0 nm and 555.0 nm with emission filters at 530/30 nm and 585/42 nm, for Alexa Fluor 488-A *vs.* AF555-A, respectively (D1 = blue distribution recorded with 488.0 nm laser excitation; and D2 = violet distribution with 555.0 nm excitation).

luminescent surface bacteria coverage, well-defined bacteria Bioimaging and individual ultraluminescent nanoparticles were recorded with equal emission intensities (inset of Fig. 5c). By red-green LUT edition of the image it was possible to corroborate/confirm homogenous ultraluminescent bacteria surface imaging (see Fig. 6d).

The non-covalent interaction of core–shell nanoparticle bacteria was explained by the polar membrane components and the hydrophilic character of the silica shell of the nanoparticles applied. From the literature, it is known that silica nanoparticles showed non-covalent interactions with *E. coli* based on their hydrophilic surface[48] composed of peptidoglycans (polysaccharides crosslinked by unusual peptides).[49] Moreover, the strength of the non-covalent interactions was explained by the combination of Wander Waals, polar interactions and hydrogen bridges of Silanols with the polar components of the membrane[50,51] to achieve the well-shaped depositions over the biosurfaces. Similarly, other types of nanoparticles, such as magneto fluorescent nanoparticles, were applied to the modification of bio-membranes of bacteria.[52]

In addition, it should be noted that the non-covalent interactions were generated/identified from nano-labellers, of 70.0 nm based on 40.0 nm gold core templates to the biostructures. Within these sizes, Wander Walls interactions should also be considered as important non-covalent interactions. From Literature about Hamaker constant[53] determinations, it was involved these types of interactions. Higher values of these constants were determined below sizes of 30 nm, accompanied with greater inter-nanoparticle interaction. While intermediate values, with higher nanoparticle size than 50 nm, lower interactions were associated. These constants correlated the nanoparticle size and their inter nanoparticle attractive potential, where it was observed that smaller sizes, in contrast to biggest ones, interact closely at shorter and longer inter-nanoparticle distances.[54] Thus, these intermediate inter-Au@SiO_2-RhB nanoparticle interactions, in addition to stronger interaction with biomembranes, allowed the accurate deposition over *E. coli*. Moreover, the Bio-MEF assay could be accurately targeted by the sole application of right laser excitation of the fluorophore and plasmonic band to record maximal MEF emissions form the deposed gold core–shell nanoplatforms on non-optical active bacteria,[55] for instance, as in cyanobacteria.[56,57] Likewise, from genetically engineered *E. coli* that produced synthetic fluorescent proteins within the membrane, their emissions were coupled and enhanced by the deposition of silver nanoparticles.[58]

In order to corroborate the deposition of the nanoparticles on *E. coli*, TEM images were recorded. The non-labelled bacteria showed low contrasted images of individual biostructures and small aggregated biostructures (Fig. 7a) due to the formation of less electro-dense bio-material. Average sizes of 1000 and 1500 nm determined from TEM image analysis correlated with Dynamic Light Scattering (DLS) measurements. This was also found in the detection/identification of small aggregates.

After the application of the nano-biolabelling methodology, nanoparticle deposition was shown on *E. coli* membranes by no-covalent interactions. The deposition of the nanolabellers on biostructures was optimized based on the variation of nanoparticle concentrations. Hence, in concentrated conditions of nanolabellers, greater interaction was seen between nanoparticles than between biostructures (Fig. 7b). Yet, by a decrease to the appropriate concentration, an improved depo-

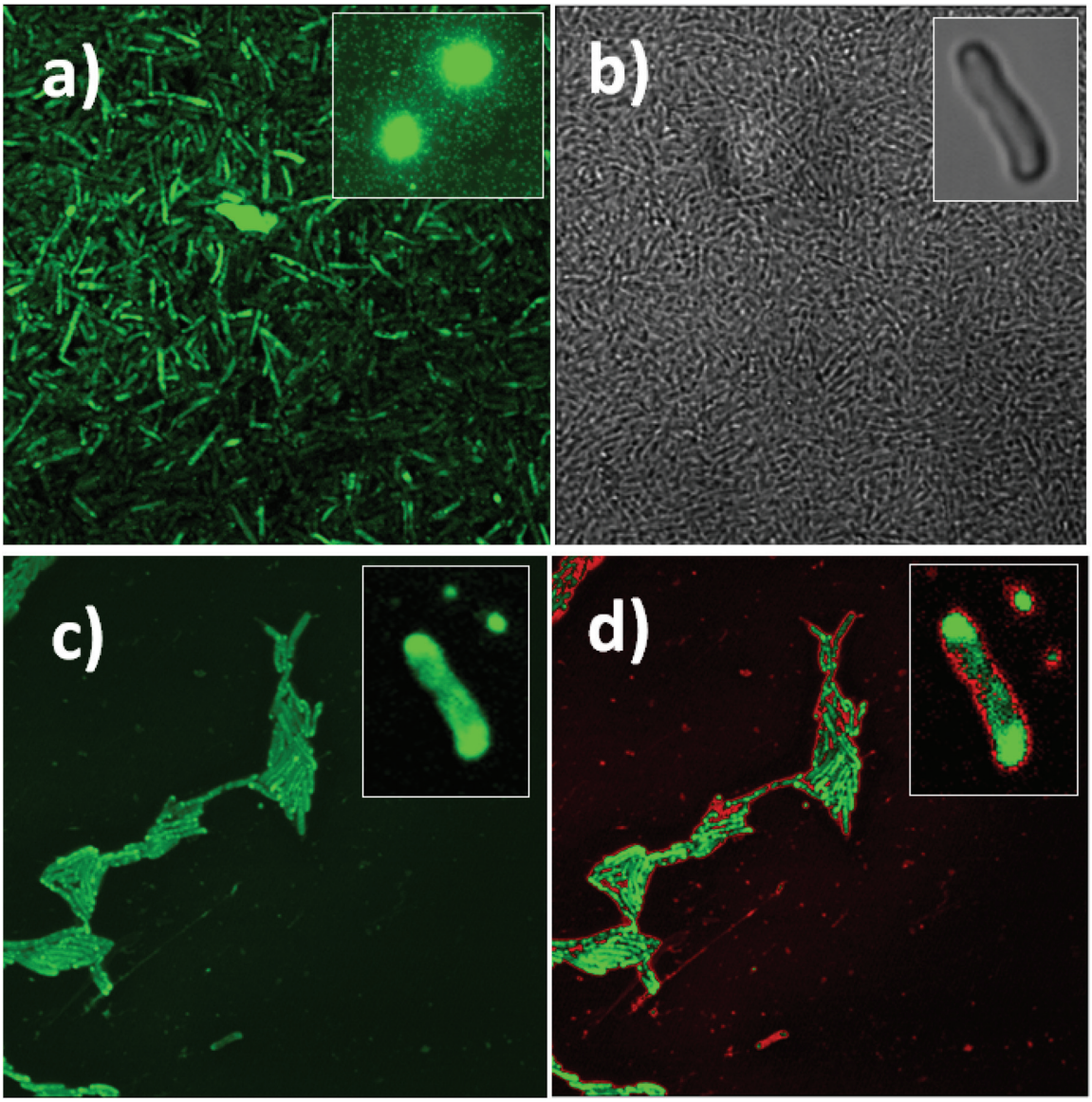

Fig. 6 (a) Aggregated *E. coli* ultraluminescent labelled at concentrated conditions by Laser Fluorescence Microscopy (optimized LUT, look at table colour edition). Inset: Ultraluminescent core–shell labellers; (b) bright field microscopy of non-labelled bacteria. Inset: Zoom of individual *E. coli*; (c) and (d) aggregated *E. coli* ultraluminescent labelled at intermedium concentration by Laser Fluorescence Microscopy with green and red-green LUT edition, respectively. Inset: Zoom of ultraluminescent *E. coli* labelled.

sition was found on the biosurfaces (Fig. 7c). Moreover, by optimizing concentrations, time of interactions and shaking, the number of nanolabeller deposition could be increased on biosurfaces leading to higher inter nano-biostructure interaction and size of aggregates (Fig. 7d).

These ultraluminescent gold core–shell nanoparticles showed excellent luminescent properties for *E. coli* biolabelling by non-covalent interactions. This observation it was recorded by Laser Fluorescence Microscopy and confirmed by TEM.

Although literature shows few approaches to fluorescent nano-labelling applications, the deposition of different nanoarchitectures was reported, such as quantum dots on *E. coli*.[59] In addition, the development of label free biosensors based on nano-engineered nanoplatforms also showed interesting applications.[60] Yet, to the best of our knowledge, developments previously reported were based on non-classical light by MEF produced from reduced sized 40 nm gold core templates from which enhanced emissions could be tuned. These enhanced emissions, generated from reduced spherical volumes in the nano-scale, were detected by in flow cytometry with laser detection with diminished photobleaching properties and higher fluorescence event detection frequency (core–shell *vs*. core-less nanoarchitectures, Fig. 4). Thus, the non-classical light mechanism found in the modified *E. coli* membranes by non-covalent interactions was highly sensitive not only based on the enhanced emission. It was also the targeted deposition by the strong non-covalent interactions

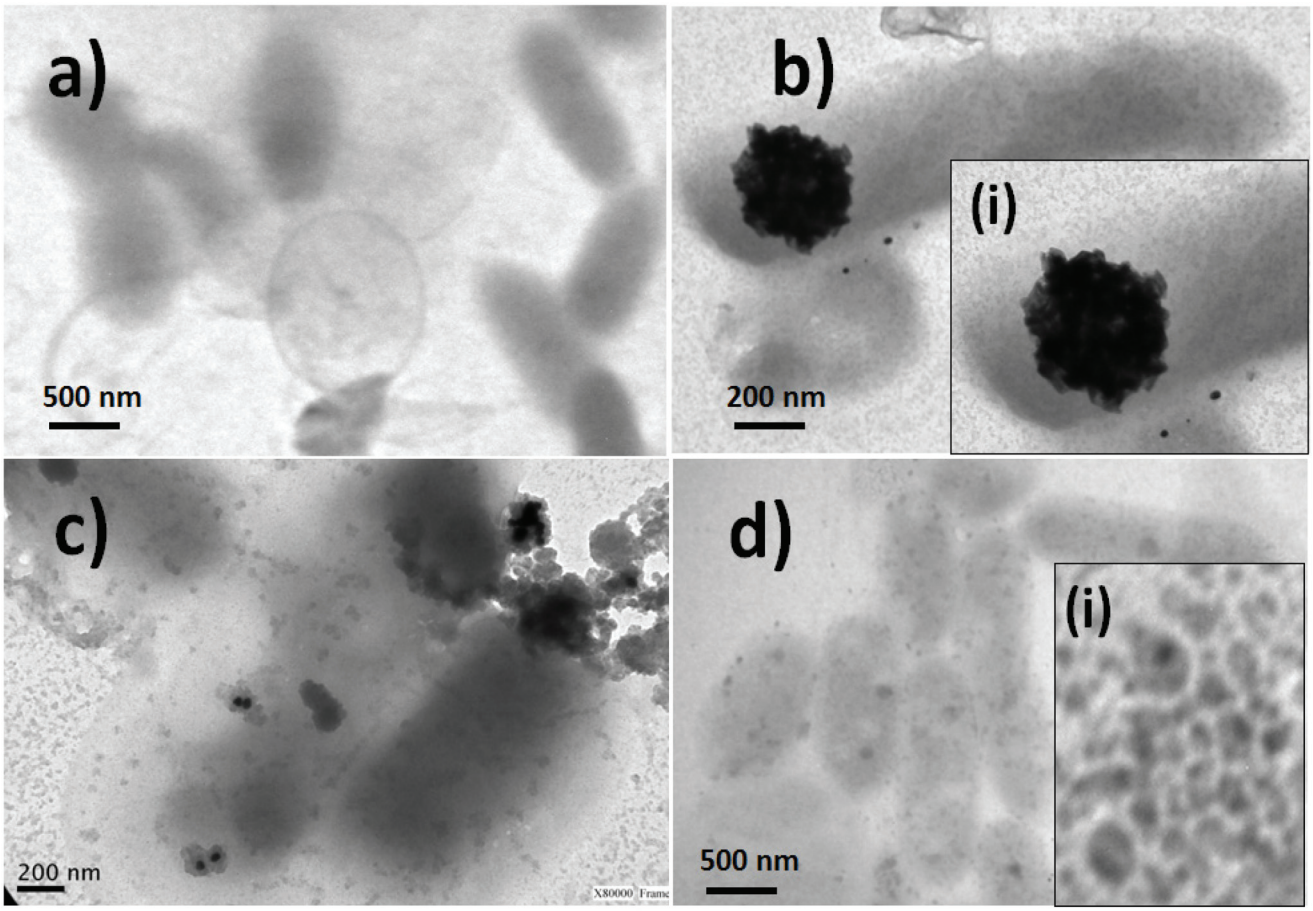

Fig. 7 TEM images of *E. coli*: (a) non-labelled biostructures; (b) modified with nanoaggregates of Au@SiO_2-RhB nanoparticles; (c) zoomed images of deposed well-dispersed Au@SiO_2-RhB nanoparticles on bacteria; (d) homogeneous nano-labelling of Au@SiO_2-RhB nanoparticles on bacteria. Inset image: zoomed image of deposed Au@SiO_2-RhB nanoparticles on biostructures.

involved and showed based on the well-shaped biostructures obtained by Laser Fluorescence Microscopy with low free nanolabellers detected in their surrounding (inset images of Fig. 6c and d). The targeted detection also improved from the formation of the nano-biostructures with ultraluminescent properties.

Then, the ultraluminescent labelled *E. coli* detection was evaluated by in flow cytometry with Laser Excitation and Fluorescence emission signaling by exploiting the MEF phenomena produced over the biostructures.

3.4 Effect of the biolabelling on the scattered light detection by in flow cytometry with laser excitation and fluorescence detection

In flow cytometry allowed the detection of individual fluorescence event counting within in flow colloidal dispersions of the nano-biostructures by laser excitation. Using this technique, different distributions of fluorescence event detection were recorded from Side-scattered light (SSC) and Forward-scattered light (FSC) plots according to the sample assayed. FSC is a measurement of mostly diffracted light, detected just off the axis of the incident laser beam in the forward direction by a photodiode. The FSC parameter provides a suitable method for detecting particles greater than a given size independent of their fluorescence; therefore it is often used in immune-phenotyping to trigger signal processing.[61] FSC is proportional to cell-surface area or size. The SSC parameter is a measurement of mostly refracted and reflected light that occurs at any interface within the cell where there is a change in refractive index.[62] SSC is collected at approximately 90 degrees to the laser beam by a collection lens and redirected by a beam splitter to the appropriate detector. Therefore, the SSC parameter is proportional to cell granularity or internal complexity.

From emission recorded by 530 nm and 650 nm filter applied, three distributions in the SSC *vs*. FSC graphs were observed. Distributions P1 (red region) and P2 (violet region) corresponds to no-labelled and labelled bacteria, respectively. Distribution P3 (blue region) corresponds to labelled bacteria collected from emission filter at 650 nm (Fig. 8a).

From SSC *vs*. Fluorescence event detection recorded with standard PerCP-A Fluorescence emitter, we can see the difference in their distributions. P1 distribution showed SSC centered at 10^4, while P2 and P3 distributions shifted to 10^5.

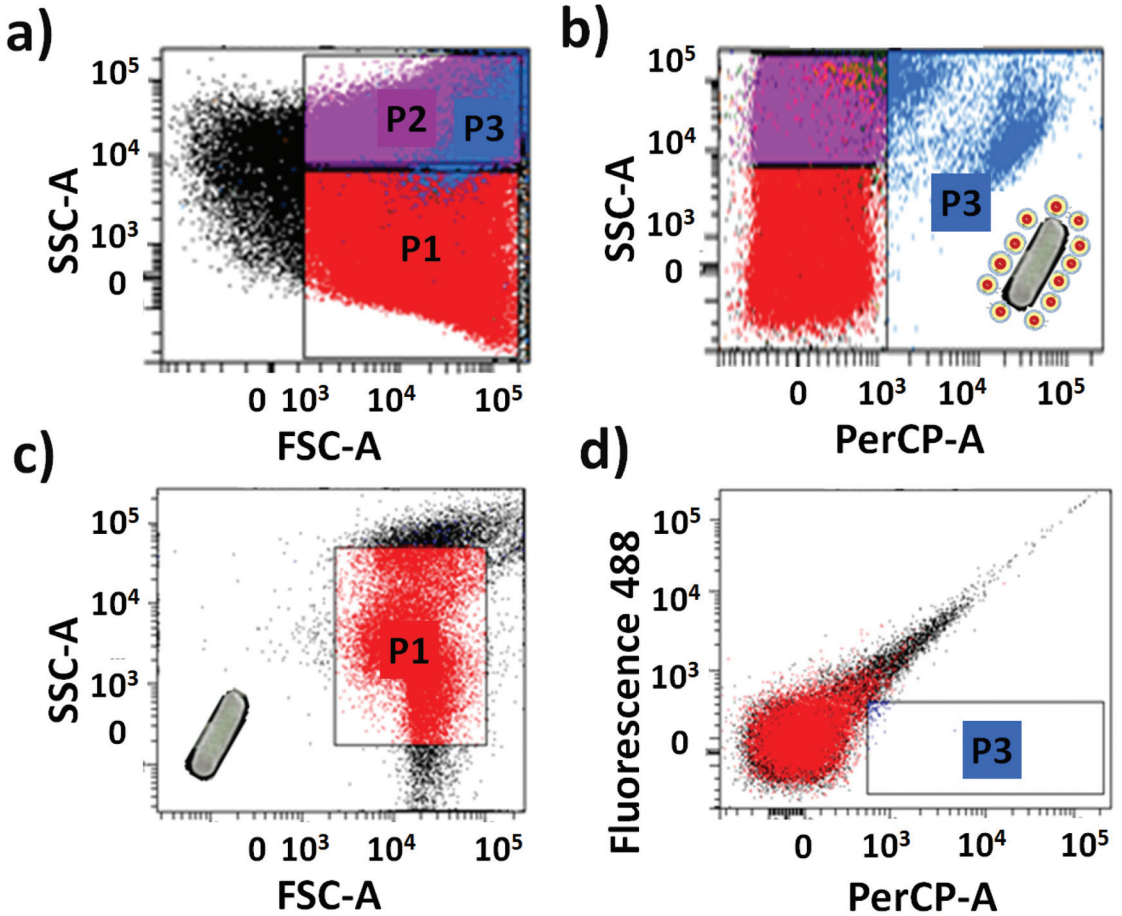

Fig. 8 In flow cytometry with laser excitation and fluorescence detection: (a) graph of Side-scattered light (SSC is proportional to cell granularity or internal complexity) *vs.* Forward-scattered light (FSC is proportional to cell-surface area or size); (b) SSC *vs.* fluorescence collected at 650 nm filter. Note: P1 (red region) and P2 (violet region) correspond to distribution of no-labelled and labelled bacteria, respectively, by collecting emission at 530 nm filter. P3 (blue region) distribution of bacteria labelled by collecting emission at 650 nm filter. Laser excitation source was at 488 nm.

Higher fluorescence event detections were detected within higher values of PerCP-A from distribution P3 (Fig. 8b). These distributions were clearly separated by the SSC parameter, within lower values centered at 10^2 for P1 and 10^4–10^5 for P2 and P3 (Fig. 7a). In addition, from SSC *vs.* PerCP-A plots, higher sizes and internal complexities were achieved from the nano-biostructures, allowing clear separation of the fluorescent event detection distribution of P3 from P2 and P1 (Fig. 8b).

As control, the non-labelled bacteria showed marked decrease of SSC and FSC distribution of values (Fig. 8c). For no-labelled bacteria fluorescence event detection counting, correlating emissions from 530 nm with 650 nm filters (Fluorescence 488 *vs.* PerCP-A plots) were sharply decreased (Fig. 8d), in relation to the highly and well-occupied fluorescence event detection distribution of labelled bacteria.

The discrimination of different distributions of fluorescence event detections corresponding to targeted nano-biostructures, non-labelled biostructures and free nanolabellers was made. This was achieved by their different responses against the laser excitation and light scattering performed, in addition to varied filter lens for detection.

In order to determine the interaction of nano-biostructures and their size, Dynamic Light Scattering (DLS) was carried out by increasing bacteria concentrations in the presence of constant Au@SiO_2-RhB nanolabeller concentration. From low to highly concentrated *E. coli* in the presence of optimal nanolabeller concentrations for biolabelling, increased sizes of nano-biostructures were found (Fig. 9a). The effect of bacteria concentration on the size of the nano-biostructures was thus assessed? At low bacteria concentrations, single nano-biostructure detection was achieved with an average size ranging from 1500 to 1600 nm, corresponding to biostructures of 1000 nm with concentrated depositions of nanolabellers and nanoaggregates, as well as 1500 nm biostructure size with homogeneous 100 nm of nanolabeller depositions. These observations and size determinations were correlated by TEM imaging. At higher bacteria concentrations, the nano-biostructures showed their interactions, increasing the size of nano-biostructure aggregates (Fig. 8a). Their interactions were

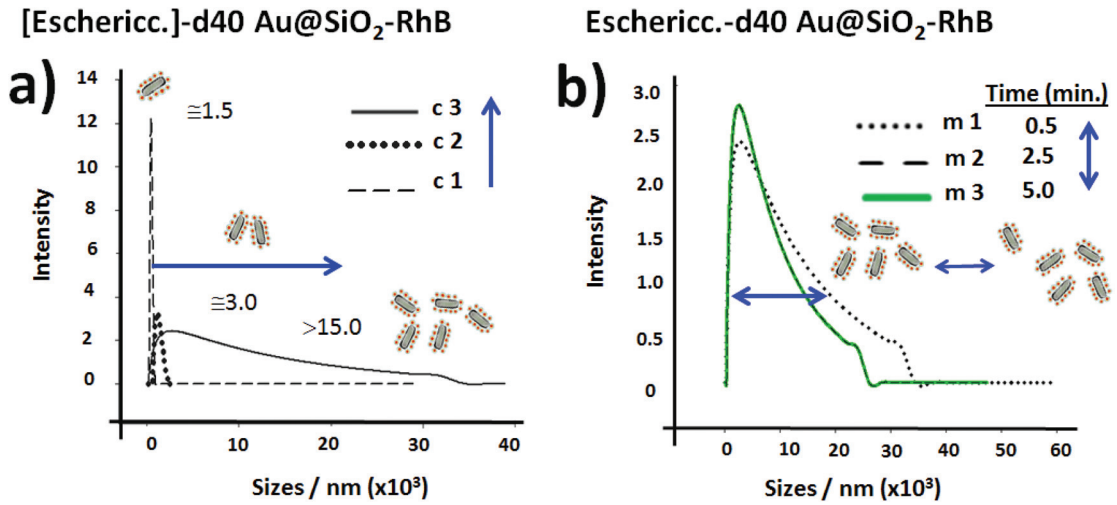

Fig. 9 Dynamic Light Scattering (DLS) of (a) optimized nano-biostructures (*E. coli*-d40 Au@SiO_2-RhB) at variable bacteria concentrations. Low and high *E. coli* concentrations (c1 and c3) corresponded to additions of 40 and 180 μL from concentrated *E. coli* bloom per ml of colloidal dispersion. (b) Size measurements within 5 minutes period of times nominated as m1, m2 and m3 for times 0.5, 2.5 and 5.0 minutes respectively.

enhanced only in the presence of nano-labellers. The size of nano-biostructures was not modified within a 10 min period, showing stability within the colloidal dispersion of the new synthetic architectures (Fig. 9b). This observation was made from the different bacteria concentrations (Fig. 9b).

In summary, the potential use of this nano-labelling methodology for detection and counting of *E. coli* biostructures from the differentiation of distribution of fluorescence event detections from labelled *E. coli* by in flow cytometry and their scattered light patterns by cytometry and DLS it was showed the.

3.5 Determination of analytical parameters of ultraluminescent *E. coli* labelling by in flow cytometry

To evaluate this nano-biolabelling methodology for the detection and quantification of *E. coli* by in flow cytometry, calibration curves were developed by variation of *E. coli* concentrations with optimized constant concentration of ultraluminescent 40 nm gold core–shell nanolabeller. Therefore, the nanolabelling methodology was applied for the different levels of bacteria concentrations. The samples were then run in the flow cytometer.

From the analysis of contour SSC *vs*. FSC plots, a proportional increase was shown in fluorescence event detection counting by increasing *E. coli* concentration from diluted concentrations (Fig. 10a) to higher concentrated colloidal dispersions added (×4 times higher) (Fig. 10b). Thus, proportional variations of the contour plots were recorded within the P3 fluorescence event detection distributions. Moreover, fluorescent event detection distribution of non-labelled bacteria was diminished, while the detected labelled bacteria distributions were increased by the increase in bacteria concentration.

The intermediate distribution of fluorescent event detection recorded from the analysis of values in SSC *vs*. FSC plots, corresponding to non-labelled bacteria, was confirmed by comparison with the scattered light distribution of standard μm beads from the BD company.

Then, the fitting model for the experimental data was analyzed. The fluorescent event detection counting against varied bacteria concentrations from the calibration curve was adjusted by a linear equation ($y = mx + b$). Thus, analytical performances were determined. An acceptable correlation coefficient (R = 0.998) was obtained for the synthetic calibration curves. The sensitivity (m) of the method was determined from the slope of the fitting equation (Fig. 11).

Variation of bacteria concentrations to higher values than those previously added to the plotting of the calibration curve in Fig. 11 led to increased dispersibility and lower values of R (R = 0.976 from Table 1). This variation was attributed to free dispersed matter within the colloidal dispersion. This new colloidal dispersion component came from the culture media at higher concentration levels. This free matter from the culture growth media of bacteria generated within the upper and intermediate distributions of SSC *vs*. FSC overlapped detection to non-labelled and labelled bacteria distributions. Thus, in order to avoid this interference, all samples were filtered and redispersed in water. Hence, a linear response with improved R values (Table 1) was obtained. The sensitivity determined considering higher levels of bacteria concentrations overlapped with the interval of the standard error values (Table 1).

In optimal conditions without matrix effect from the culture growth media, it was possible to record the dynamics of nano-biostructure formation from the different fluorescent event detection distributions based on non-covalent interactions. Here, the following observations should be made: (a) smaller sizes of the nano-labellers detected in the lower and intermediate SSC *vs*. FSC region of values showed variation in the number of fluorescent event detections depending on bacteria concentration; and (b) it was possible to record the dim-

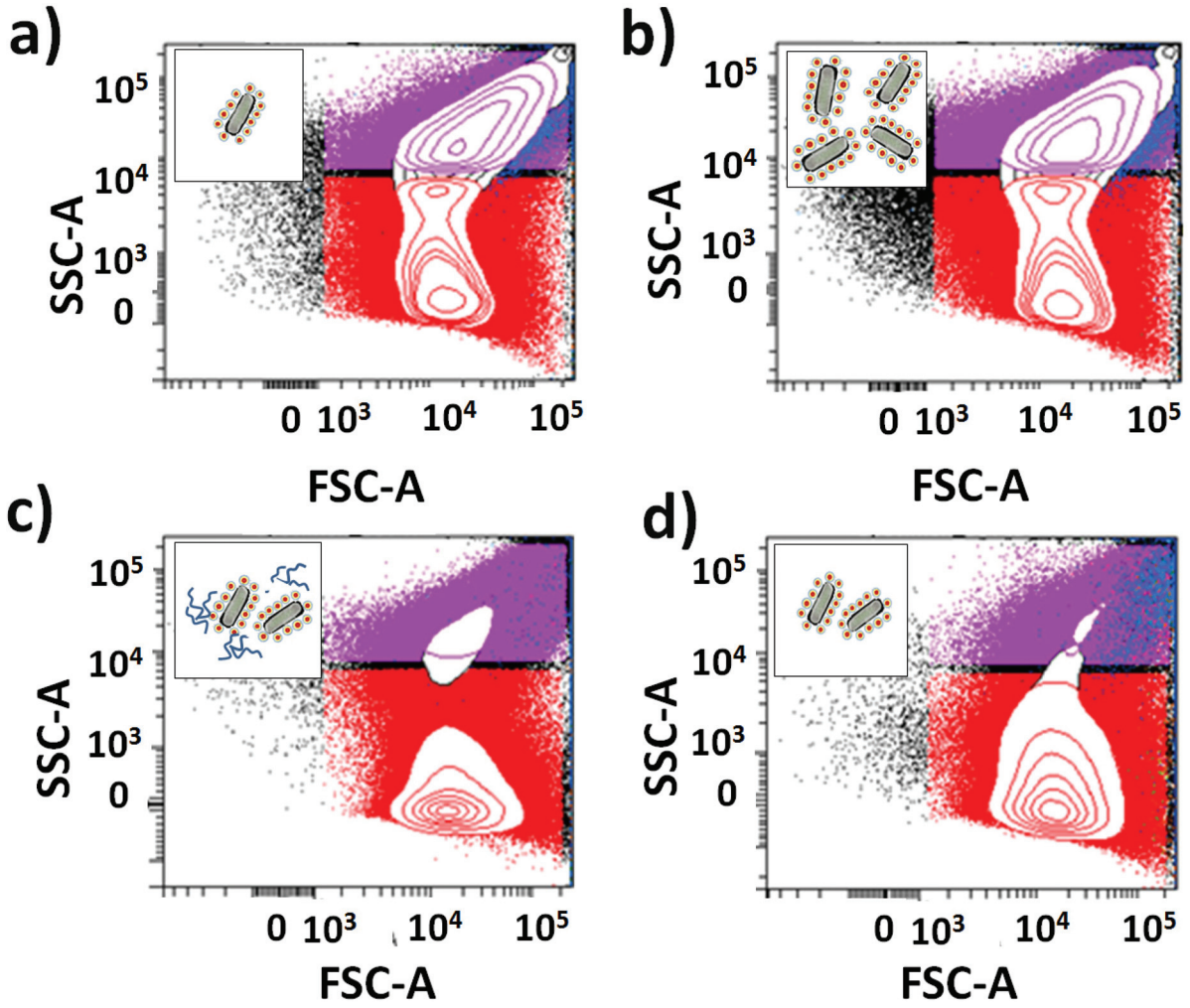

Fig. 10 In flow cytometry with laser excitation and fluorescence detection. Graphs of Side-scattered light (SSC is proportional to cell granularity or internal complexity) *vs*. Forward-scattered light (FSC is proportional to cell-surface area or size): (a) diluted labelled *E. coli*; (b) concentrated labelled *E. coli*; (c) *E. coli* labelled from fortified water sample; (d) sample of filtrated *E. coli* labelled from fortified water. P1 (red region) and P2 (violet region) correspond to distribution of no-labelled and labelled bacteria, respectively, [commas] by collecting emission at 530 nm filter. P3 (blue region) distribution of bacteria labelled by collecting emission at 650 nm filter. Laser excitation source was at 488 nm.

inution in the distributions from lower and intermediate SSC *vs*. FSC values (assigned to free nano-labellers and non-labelled bacteria) to increasing values within the labelled *E. coli* distributions in the upper distribution region. The dynamics of the nano-biosystem thus allowed the detection and quantification of nano-biostructures.

3.6 Quantification and validation in aqueous media

Then, in order to quantify *E. coli*, synthetic real samples of fortified tap water were prepared with known concentration additions. This matrix was chosen as a representative biological aqueous media that could be obtained from varied real samples such as serum,[63] urine,[64–66] fruits[67] and milk.[68] Moreover, it was considered as a medium for the development of new approaches for in flow detection, imaging, and treatment.[69] In this way, additions were regarded within the linear interval of concentrations in the calibration curve.

The concentrations were checked by the traditional bacteria counting by Bright Field Transmission Microscopy. It was possible to detect and quantify different concentrations of labelled *E. coli* with acceptable statistical % Coefficient of Variation (%CV) values by applying the developed methodology based on MEF nano-biolabelling. The determined CV % values were within 97–99% in replicates of the same concentration level. From these values the precision and accuracy of the methodology was confirmed by in flow cytometry. However, we should mention the high sensitivity against variation of the media in the methodology developed. For tap water as a real matrix, a matrix effect was also observed from fortified matrix samples with *E. coli*.

The nano-biolabelling within tap water caused higher aggregates with opalescence in the colloidal dispersion. This could be attributed to a different ionic strength, mineral composition and eventual dispersed dust. SSC *vs*. FSC plots

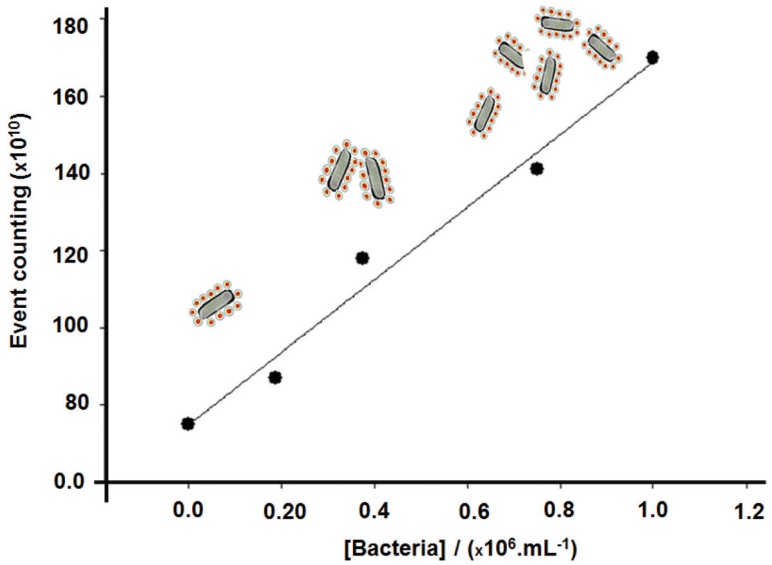

Fig. 11 Calibration curve of bacteria labelled with core–shell nanoparticles by cytometry with fluorescence detection.

Table 1 Analytical parameters of *E. coli* detection from calibration curves

Analytical parameters[a]	Value	Standard error[e]	R^f
$m^{b,c}$	94.0	7	0.9906
b^c	74	4	
$m^{b,d}$	92	14	0.9763
b^d	45	6	

[a] Analytical parameters obtained by linear regression $y = mx \times b$. [b] Sensitivity of the calibration curve corresponds to m. [c] Filtrated samples. [d] Non-filtrated samples. [e] Standard error determined from the standard deviation of residuals. [f] Correlation coefficient.

showed distributions of fluorescence event detection counting in the P3 region (Fig. 10c) higher than those in the absence of the real matrix. The higher P3 distribution of fluorescence event detection counting was accompanied with a decrease the P1 region. This was related to the increase in the inter-nano-biostructure interactions in the presence of the tap water media that increased P3 distribution and decreased P1.

In the presence of the tap water interference, a hydrophobic effect and increased interactions between polar silanized nano-biostructures were caused by hydrogen bridges.[70] These non-covalent interactions phenomena explained the increase of the P3 region from the greater interactions of non-labelled bacteria and nanolabellers, increasing P3 region and decreasing the P1 one. This effect was lessened/mitigated/softened in the presence of filtrated tap water, showing lower P3 distribution and increased P1.

The matrix effect was eliminated by the use of filtrated tap water for nano-biolabelling. Thus, the positive matrix effect observed by SSC *vs.* FSC contour plots (Fig. 10d) was removed. Therefore, interferences were eradicated. The quantification was carried out with acceptable statistical parameter of accuracy (standard deviation, s) and precision (% Coefficient of Variation, %CV).[71]

Then, in order to validate the in flow cytometry quantification in tap water with the nano-biolabelling methodology developed, the fortified samples were quantified by a standard cell counter with fluorescence detection for biochemical analysis. Therefore, it was possible to detect well-shaped Gaussian distributions in the entire linear interval of the bacteria concentrations assayed. For example, in the level of concentration analyzed and discussed previously by in flow cytometry, a Gaussian Fluorescence event detection distribution was observed, along with a small overlapped band corresponding to non-labelled bacteria and free nano-labellers (Fig. 12a). The optical transparent non-labelled *E. coli* showed smaller Gaussian detection bands, as well as free nano-labellers (Fig. 12b).

Thus, for quantifications made with the cell counter, we considered the subtraction of the blanks of the free nano-labellers and non-labelled bacteria that allowed determining a concentration of 0.6×10^6 bacteria per ml with a %CV of 3–5 from triplicates. The values obtained correlated with the interval of values recorded from in flow cytometry ($0.6–0.7 \times 10^6$ bacteria per ml) (Table 2).

Moreover, this bacteria counting was correlated by Laser Fluorescence Microscopy. To do so, the well-known standard technique of cell counting was performed with Bright Field Transmission Microscopy on Cell counting glass chamber slides. The results of ultraluminescent labelled *E. coli* counting showed similar values to those indicated by other methodologies ($0.5–0.6 \times 10^6$ bacteria per ml) (Table 2). However it should be noted that the lower interval of values recorded

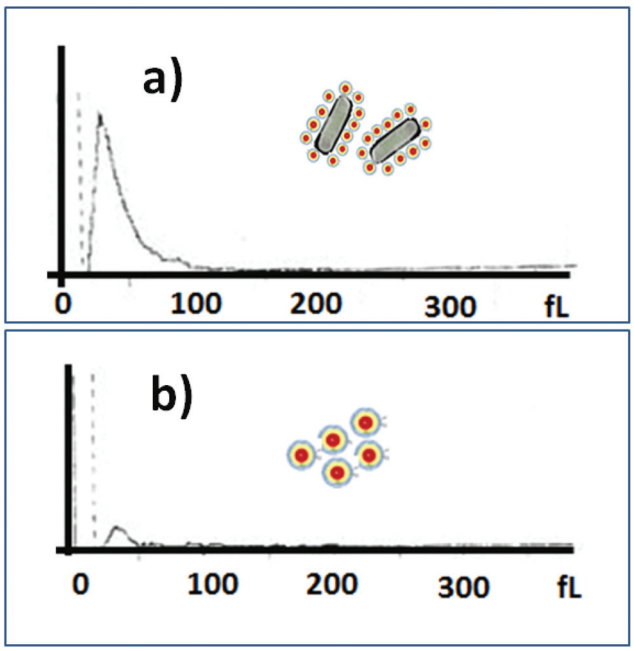

Fig. 12 Bacteria quantification by a cell counter with fluorescent detection: (a) detection of *E. coli* labelled by Au@SiO_2-RhB; (b) detection of nano-labeller Au@SiO_2-RhB nanoparticles.

Table 2 *E. coli* counting by different methodologies

Methodology[a]	[Bacteria] × 10^6/ bacterium per mL	σ^e
Cytometry[b]	0.60–0.70	0.07
Bacteria counter[c]	0.6	0.1
Fluorescence microscopy[d]	0.50–0.60	0.04

[a] Dilution 1/100 from concentrated bacteria dispersion. [b] In flow cytometry with laser 488 nm excitation. [c] Bacteria counter with fluorescence detection. [d] Bacteria counting over glass slide with Laser Fluorescence Microscopy. [e] Standard deviation of the fluorescent event detection counting recorded within the interval of values assayed based on developed Bio-MEF assay.

resulted from the homogeneous ultraluminescent nano-biostructures considered, while partial or low emission was not taken into account.

Intra-assays of bacteria counting by in flow cytometry showed lower standard deviations (σ = 0.07) compared to the standard counter used (σ = 0.1) (Table 2). Thus, the precision was higher by the methodology developed on the basis of the Bio-MEF assay. However, by in Fluorescence Microscopy, the Bio-MEF assay allowed lower standard deviation of intra-assays (σ = 0.04) (Table 2). This was ascribed to the intrinsic methodology characteristics based on imaging generated by ultraluminescent biostructures. Yet, it should be noted that the use of in flow cytometry was less time consuming with more information acquisition from single fluorescent detection events with acceptable statistical and analytical performance parameters. This Bio-MEF assay showed potential applications for imaging in flow cytometry[72] and new optical coupled approaches[73] as well.

3.7 Evaluation of the limit of bacteria detection (LBD)

Then, in order to determine the Limit of Bacteria Detection (LBD), concentrations of *E. coli* were decreased within aqueous media in low value intervals where single bacteria detection levels could be evaluated. From a higher dilution factor applied (1/1 × 10^5) to the concentrated colloidal dispersion used for the plotting of the calibration curve, this phenomenon was experimentally evaluated. In this manner, Bio-MEF assay was compared by In Flow Cytometry, Laser Fluorescence Microscopy and Confocal Bright Field Microscopy. Thus, the In Flow Bio-MEF assay showed a low number of fluorescent detection events within the intervals of bacteria concentrations 0.2–0.4 × 10^2 bacterium per mL. Hence, detected low fluorescent detection events were visible within these low bacteria concentrations intervals (Fig. 13a and b), distinguishing these Bio-MEF phenomena detection after addition of small aliquots (addition of 50 μL from dilution 1/1 × 10^5 of concentrated colloidal dispersion) from the diluted *E. coli* colloidal dispersion (Fig. 13c and d).

The standard deviation of intra-assays within this low bacteria concentration interval was centered at 45 ± 10 bacteria and intra-assays 80 ± 20 Bacteria (Table 3). From non-labelled bacteria considering the scattered light for detection event counting, a higher dispersion in the bacteria counting was generated (Table 3). The values determined by in flow Bio-MEF assay correlated with counting obtained by Laser Fluorescence Microscopy. However, based on Bio-MEF imaging, single Ultraluminescent bacteria detection was achieved within lower intervals of concentrations as previously reported by us.

A LBD of 250 was estimated by in flow cytometry Bio-MEF assay, while single bacterium detection was determined by Laser Fluorescence Microscopy. Yet, it should be noted the faster and effective methodology developed within in flow cytometry in comparison to detection of individual biostructures by optical detection. In addition, non-labelled bacteria counting showed no proportional correlations with the number of concentrations assayed. Therefore, we showed the potential applications of the coupling of both techniques based on MEF.

Finally, the low LBD determination was based on experimental manipulations of the decreasing sample volumes and concentrations for testing real detection events. This approach developed by manipulating the conditions assayed was consistent with many intra-assays developed. However, considering the definition of Limit of Detection (LOD) for chemical sensing ($3 \times \sigma/m$),[74] low acceptable and reproducible values were not obtained due to greater variations incorporated into the blanks.

An Ultraluminescent nano-biolabelling methodology was applied on the basis of Bio-MEF properties of 40 nm gold

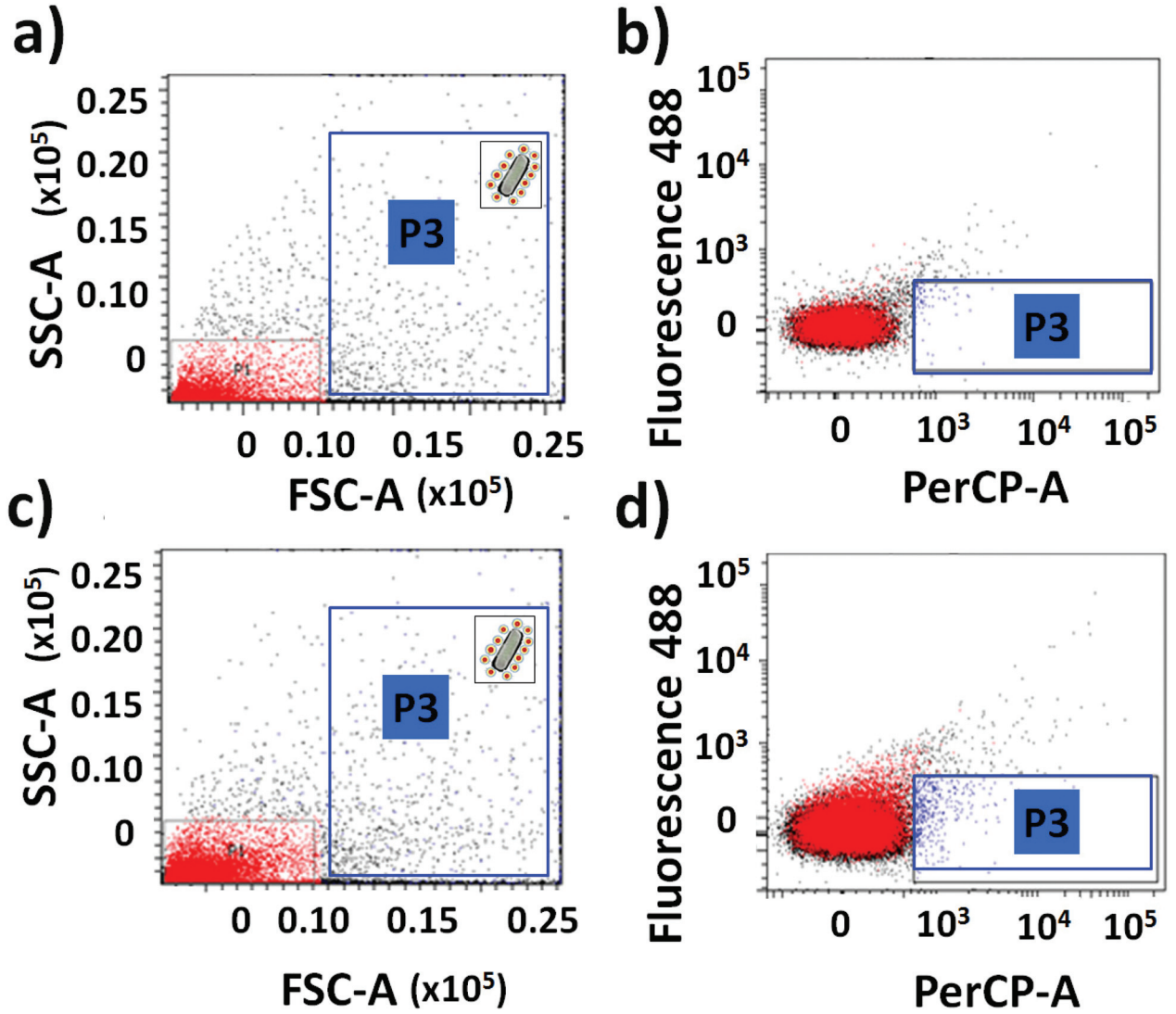

Fig. 13 Limit of Bacteria Detection (LBD) for *E. coli* by in flow cytometry with laser excitation and fluorescence detection: (a) SSC *vs*. FSC plots within lower bacteria concentration (addition of 50 μL from dilution 1/1 × 10^5 of concentrated colloidal dispersion); (b) fluorescence 488 collected with 530 nm filter *vs*. fluorescence collected at 650 nm filter within lower bacteria concentration (addition of 50 μL from dilution 1/1 × 10^5 of concentrated colloidal dispersion); (c) SSC *vs*. FSC plots within modified increase of lower bacteria concentrations (addition of 2× aliquotes of 50 μL from dilution 1/1 × 10^5 of concentrated colloidal dispersion within the previous sample (a)); (d) fluorescence 488 collected with 530 nm filter *vs*. fluorescence collected at 650 nm filter modified increase of lower bacteria concentrations (addition of 2× aliquotes of 50 μL from dilution 1/1 × 10^5 of concentrated colloidal dispersion within the previous sample (a)).

core–shell nanoparticles for in flow cytometry for detection and quantification of *E. coli*. This methodology coupled to the analysis of the main parameters of cytometry from light scattering recorded with laser excitation allowed distinguishing the distribution of fluorescence event detection counting from labelled *E. coli*, non-labelled bacteria and free nano-labellers. The detection of single fluorescence events of μm size was thus demonstrated from collective emissions of non-covalent nano-labellers deposed on *E. coli*. Enhanced emissions were also generated from 40 nm gold core templates by in flow laser excitation and coupling with their emitters placed on their surrounding with an accurate control of spacer shell lengths. Non-classical light was generated by MEF within in flow methodology not reported previously. Individual ultraluminescent nano-biostructures were recorded by in flow cytometry and Laser Fluorescence Microscopy.

These results showed that this methodology can be potentially applied to Confined Microfluidics Chips[75] for Biodetection and Biophotonic applications in low bacteria concentrations and single biostructure detection.[76] Additionally, their hydroxylated nanoparticle surfaces based on silica shell coverage allow the chemical modification and bioconjugation to be applied to cells and organelle interactions.[77] Further experiments in this way aim at providing insights into nanoparticles and bio-interactions for Bioimaging and drug delivery applications.

Table 3 Determination of Limit of Bacteria Detection (LBD) by methodologies based on Bio-MEF assays

Methodology[a]	Bio-assay[b]	[Bacteria][c] × 10^2/ bacterium per mL	σ_{intra}[d]	σ_{inter}[e]	LBD[f]
In flow cytometry[g]	Bio-MEF assay[h]	0.2–0.4	45 ± 10	80 ± 20	250
	Non-labelled bacteria control[i]	0.2–0.4	50 + 20	100 + 45	400
Fluorescence microscopy[j]	Bio-MEF assay[h]	0.05–0.1	(–)	(–)	1–10

[a] Methodologies used for fluorescent event detection counting. [b] Bio-assays used for fluorescent event detection. [c] Bacterium detected per mL of colloidal dispersion. [d] Standard deviation between intra-assays corresponded to triplicates at the same concentration with ±standard error. [e] Average values of standard deviation between inter-assays recorded at different concentrations within low bacteria concentration intervals. Increases of 50 μL additions from 1/1 × 10^5 dilution of concentrated bacteria dispersion were used. The average was obtained from 4 additions. [f] Limit of Bacteria Detection (LBD). Values lower than LBD were considered by light scattered detection. [g] Laser excitation used was 488.0 nm and emission recording was by 530 and 650 nm filters. [h] Bio-MEF assay was based on the Ultraluminescent nano-biolabelling developed with Au@SiO_2-RhB nanoparticles. [i] Control sample of non-labelled bacteria used at the same low concentration interval applied. [j] Laser Fluorescence Microscopy with 488 nm excitation.

4. Conclusions

Ultraluminescent gold core–shell nano-labellers were developed from MEF for *E. coli* detection and quantification by in flow cytometry with laser excitation and fluorescence detection. The Bio-MEF assay allowed, from non-optical active biostructures, ultraluminescent nano-biostructure detection within in flow cytometry and imaging by Laser Fluorescence Microscopy. The in flow Bio-MEF assay showed to be a less time consuming methodology. In addition, well-resolved bioimaging was recorded by Laser Fluorescence Microscopy, showing potential applications for imaging in flow methodologies. This Bio-MEF methodology was successfully validated by other traditional cell counting methods. However, the ultraluminescence properties were based on MEF from 40 nm gold core templates accurately silanized and fluorescent modified for optimized emissions. Thus, by controlling the laser excitation for optimal fluorophore-plasmonic coupling, enhanced emissions were recorded from the modified nano-biosurfaces. The Silanol groups of the silica shells enabled the non-covalent interaction and deposition on the *E. coli.* Thus, only well-shaped individual bright ultraluminescent biostructures were recorded with a low number of free nano-labeller detections by optimizing their concentrations.

In this manner, different fluorescence event detection distributions were recorded by in flow cytometry with laser excitation, fluorescence detection and by scattered light analysis of labelled *E. coli*, non-labelled biostructures and free nanoemitters. From the analysis of the different distributions of fluorescence event detection counting, a methodology was developed to detect and quantify *E. coli*. Experimental data were recorded from the calibration curve fitted to a linear equation. Sensitivity was determined from the slope of the calibration curve, enabling the quantification of fortified tap water samples with *E. coli*. However, the matrix samples modified the distribution of the fluorescence event detections that produced higher dispersibility in the detection values recorded. The matrix effect was eliminated by the filtration of water samples. Accordingly, the fortified samples were quantified with acceptable statistical parameters of accuracy and precision. The developed nano-biolabelling methodology was validated with the standard cell counter, and bacteria counting was validated with Bright Field Microscopy and Laser Fluorescence Microscopy.

This Bio-MEF assay allowed low nano-biostructure detection and quantification. The Limit of Bacteria Detection (LBD) value was 250 bacteria per ml by in flow cytometry, while 1 to 10 bacteria by Laser Fluorescence Microscopy.

The detection of individual enhanced fluorescence event detections based on the collective emissions of 40 nm gold core–shell nanoparticles deposed on *E. coli* by non-covalent interactions produced non-classical synthetic bio-ultraluminescent properties. Therefore, potential applications within confined microfluidics towards nanofluidics could be developed from these nanoplatforms.

Conflicts of interest

There are no conflicts to declare.

Acknowledgements

We would like to acknowledge the grants and funds provided to accomplish this work. We would also like to particularly thank SeCyT (Secretary of Science and Technology from the National University of Cordoba, UNC, Argentina) for the first grant for Young Researchers.

Thanks to Dr Paula Abadie and Dr Pilar Crespo should also be given for their assistance, from the Laboratory of Cytometry, Research Center of Biochemistry and Immunology, Department of Biochemistry, National University of Cordoba, Argentina (Centro de Investigaciones en *Bioquímica Clínica* e Inmunología, *CIBICI-CONICET*). We would also like to thank the Clinical and Bacteriological Analysis Laboratory for biomanipulations and validation assays (Laboratorio de Análisis Clínicos y Bacteriológicos, Clínica de la Familia II, Río Tercero, Argentina).

Finally, we are grateful to Professor Denis Boudreau from Département de Chimie and Centre d'Optique, Photonique et Laser, Québec, Canada, for collaborative research work in progress related to Nanophotonics and Biophotonics; as well as to all the Canadian Grants that permit it.

References

1 D. Aebisher, D. Bartusik and J. Tabarkiewicz, Laser flow cytometry as a tool for the advancement of clinical medicine, *Biomed. Pharmacother.*, 2017, **85**, 434–443.
2 W. K. W. Li and P. M. Dickie, Monitoring Phytoplankton, Bacterioplankton, and Virioplankton in a Coastal Inlet (Bedford Basin) by Flow Cytometry, *Cytometry*, 2001, **44**, 236–246.
3 L. Bernard, C. Courties, C. Duperray, H. Schafer, G. Muyzer and P. Lebaron, A New Approach To Determine the Genetic Diversity of Viable and Active Bacteria in Aquatic Ecosystems, *Cytometry*, 2001, **43**, 314–321.
4 A. E. Depince-Berger, C. Aanei, M. Iobagiu, M. Jeraiby and C. Lambert, New tools in cytometry, *Morphologie*, 2016, **33**, 199–209.
5 T. Bouvier, M. Troussellier, A. Anzil, C. Courties and P. Servais, Using Light Scatter Signal to Estimate Bacterial Biovolume by Flow Cytometry, *Cytometry*, 2001, **4**, 188–194.
6 V. P. Zharov, E. I. Galanzha, E. V. Shashkov, J.-W. Kim, N. G. Khlebtsov and V. V. Tuchin, Photoacoustic flow cytometry: principle and application for real-time detection of circulating single nanoparticles, pathogens, and contrast dyes in vivo, *J. Biomed. Opt.*, 2007, **12**(5), 051503.
7 J. Porter, D. Deere, R. Pickup and C. Edwards, Fluorescent Probes and Flow Cytometry: New Insights Into Environmental Bacteriology, *Cytometry*, 1996, **23**, 91–96.
8 D. Yu, M. A. Baird, J. R. Allen, E. S. Howe, M. P. Klassen, A. Reade, K. Makhijani, Y. Song, S. Liu, Z. Murthy, S.-Q. Zhang, O. D. Weiner, T. B. Kornberg, Y.-N. Jan, M. W. Davidson and X. Shu, A naturally monomeric infrared fluorescent protein for protein labeling in vivo, *Nat. Methods*, 2015, **12**(8), 763–765.
9 S. Vira, E. Mekhedov, G. Humphrey and P. S. Blank, Fluorescent labeled antibodies - balancing functionality and degree of labeling, *Anal. Biochem.*, 2010, **402**(2), 146–150.
10 T. Terai and T. Nagano, Small-molecule fluorophores and fluorescent probes for Bioimaging, *Pflugers Arch.*, 2013, **465**(3), 347–359.
11 C. Piñero-Lambea, G. Bodelón, R. Fernández-Periáñez, A. M. Cuesta, L. Álvarez-Vallina and L.Á Fernández, Programming, Controlled Adhesion of *E. coli* to Target Surfaces, Cells, and Tumors with Synthetic Adhesins, ACS Synthetic Biology, *ACS Synth. Biol.*, 2015, **4**, 463–473.
12 R. Ibáñez-Peral, P. L. Bergquist, M. R. Walter, M. Gibbs, E. M. Goldys and B. Ferrari, Potential Use of Quantum Dots in Flow Cytometry, *Int. J. Mol. Sci.*, 2008, **12**, 2622–2638.
13 C. M. MacLaughlin, N. Mullaithilaga, G. Yang, Y. Shell, C. Wang and G. C. Walker, Surface-Enhanced Raman Scattering Dye-Labeled Au Nanoparticles for Triplexed Detection of Leukemia and Lymphoma Cells and SERS Flow Cytometry, *Langmuir*, 2013, **29**, 1908–1919.
14 D. Brouard, M. Lessard-Viger, A. G. Bracamonte and D. Boudreau, Label-free biosensing based on multilayer fluorescent nanocomposites and a cationic polymeric transducer, *ACS Nano*, 2011, **5**, 1888–1896.
15 D. Boudreau, *et al.*, Patented Capillary Device and Process for Fabricating Thereof, *United States Patent* US10094762B2, 2018.
16 M. Rioux, D. Gontero, A. V. Veglia, A. Guillermo Bracamonte and D. Boudreau, Synthesis of Ultraluminiscent gold core-shell Nanoparticles as NanoImaging Platforms for Biosensing applications based on Metal enhanced fluorescence, *RSC Adv.*, 2017, **7**, 10252–10258.
17 D. Gontero, A. V. Veglia, D. Boudreau and A. Guillermo Bracamonte, Ultraluminescent gold Core@shell nanoparticles applied to individual bacterial detection based on Metal-Enhanced Fluorescence Nanoimaging, *J. Nanophotonics*, 2018, **12**(1), 012505.
18 M. L. Viger, L. S. Live, O. D. Therrien and D. Boudreau, Reduction of Self-Quenching in Fluorescent Silica-Coated Silver Nanoparticles, *Plasmonics*, 2008, **3**, 33–40.
19 J. Asselin, P. Legros, A. Grégoire and D. Boudreau, Correlating metal-enhanced fluorescence and structural properties in Ag@ SiO_2 Core-shell nanoparticles, *Plasmonics*, 2016, **11**(5), 1369–1376.
20 M. Rioux, D. Gontero, A. V. Veglia, A. G. Bracamonte and D. Boudreau, Synthesis of Ultraluminiscent gold core-shell Nanoparticles as NanoImaging Platforms for Biosensing applications based on Metal enhanced fluorescence, *RSC Adv.*, 2017, **7**, 10252–10258.
21 J. R. Lackowicz, Radiative decay engineering 5: metal-enhanced fluorescence and plasmon emission, *Anal. Biochem.*, 2005, **337**, 171–194.
22 C. D. Geddes and J. R. Lakowicz, Metal-Enhanced Fluorescence, *J. Fluoresc.*, 2002, **12**(2), 121–129.
23 C. Graf, D. L. J. Vossen, A. Imhof and A. van Blaaderen, A General Method to Coat Colloidal Particles with Silica, *Langmuir*, 2003, **19**, 6693–6700.
24 D. Paramelle, A. Sadovoy, S. Gorelik, P. Free, J. Hobley and D. G. Fernig, A rapid method to estimate the concentration of citrate capped silver nanoparticles from UV-visible light spectra, *Analyst*, 2014, **139**, 4855.
25 J. McFarland, Nephelometer: An Instrument for Estimating the Number of Bacteria in Suspensions Used for Calculating the Opsonic Index and for Vaccines, *J. Am. Med. Assoc.*, 1907, **14**, 1176–1178.
26 A. Turano and F. Pirali, Quantification Methods in Microbiology, in *Laboratory Diagnosis of Infectious Diseases*, ed. A. Balows, W. J. Hausler, M. Ohashi, A. Turano and E. H. Lennete, Springer, New York, NY, 1988.
27 Y. Roiter, M. Ornatska, A. R. Rammohan, J. Balakrishnan, D. R. Heine and S. Minko, Interaction of Nanoparticles with Lipid Membrane, *Nano Lett.*, 2008, **8**, 941–944.

28 S. E. A. Gratton, P. A. Ropp, P. D. Pohlhaus, J. C. Luft, V. J. Madden, M. E. Napier and J. M. DeSimone, *Proc. Natl. Acad. Sci. U. S. A.*, 2008, **105**, 11613, 11618.
29 B. V. Enustun and J. Turkevich, Coagulation of Colloidal Gold, *J. Am. Chem. Soc.*, 1963, **85**(21), 3317–3328.
30 C. J. Brinker and G. W. Scherer, Sol-Gel Science, *The Physics and Chemistry of Sol-Gel Processing*, Academic Press, Inc. An Imprinted of Elsevier, 1990, ISBN:13–978–0–12–134970–7.
31 L. M. Liz-Marzn, M. Giersig and P. Mulvaney, Synthesis of Nanosized Gold–Silica Core–Shell Particles, *Langmuir*, 1996, **12**(18), 4329–4335.
32 D. Brouard, M. Lessard-Viger, A. G. Bracamonte; and D. Boudreau, Label-free biosensing based on multilayer fluorescent nanocomposites and a cationic polymeric transducer, *ACS Nano*, 2011, **5**, 1888–1896.
33 A. V. Veglia and A. G. Bracamonte, Metal Enhanced fluorescence emission and Quenching protection effect with a host-guest Nanophotonic-supramolecular structure, *J. Nanophotonics*, 2018, **12**(3), 033004.
34 M. L. Viger, L. S. Live, O. D. Therrien and D. Boudreau, Reduction of Self-Quenching in Fluorescent Silica-Coated Silver Nanoparticles, *Plasmonics*, 2008, **3**, 33–40.
35 J. R. Lackowicz, Radiative decay engineering: Metal enhanced fluorescence and plasmon emission, *Anal. Biochem.*, 2005, **337**, 171–194.
36 C. D. Geddes, Metal-enhanced fluorescence, *Phys. Chem. Chem. Phys.*, 2013, **15**, 19537.
37 J. Asselin, P. Legros, A. Grégoire and D. Boudreau, Correlating Metal-Enhanced Fluorescence and Structural Properties in $Ag@SiO_2$ Core-Shell Nanoparticles, *Plasmonics*, 2016, 1–8.
38 E. Abbe, *Arch. Mikrosk. Anat.*, 1873, **9**, 413.
39 D. Axelrod, Selective imaging of surface fluorescence with very high aperture microscope objectives, *J. Biomed. Opt.*, 2001, **6**(1), 6–13.
40 L. Bergstrom, Hamaker constants of inorganic materials, *Adv. Colloid Interface Sci.*, 1997, **70**, 125–169.
41 K. Jiang and P. Pinchuk, Temperature and size-dependent Hamaker constants for metal nanoparticles, *Nanotechnology*, 2016, **27**, 345710.
42 C. Liu and C. E. Capjack, Effects of cellular fine structure on scattered light pattern, *IEEE Trans. Nanobioscience*, 2006, **5**(2), 76–82.
43 P. Lin, R. Owens, G. Tricot and C. S. Wilson, Flow Cytometric Immunophenotypic Analysis of 306 Cases of Multiple Myeloma, *Am. J. Clin. Pathol.*, 2004, **121**, 482–488.
44 G. Bellemare, R. J. Cedergren and G. H. Cousineau, Comparison of the Physical and Optical properties of Escherichia Coli and Sea Urchin 5 s Ribosomal RNAs, *J. Mol. Biol.*, 1972, **68**, 445–454.
45 Y. Hu, N. Zhao, T. Gan, J. Duan, H. Juan Yu, D. Meng, J. Liu and W. Liu, Analytic Method on Characteristic Parameters of Bacteria in Water by Multiwavelength Transmission Spectroscopy, *J. Spectrosc.*, 2017, **2017**, 4039048.
46 D. Campbell, V. Hurry, A. K. Clarke, P. Gustafsson and G. Oquist, *Microbiol. Mol. Biol. Rev.*, 1998, **62**(3), 667–683.
47 T. S. Moore, C. B. Mouw, J. M. Sullivan, M. S. Twardowski, A. M. Burtner, A. B. Ciochetto, M. N. McFarland, A. R. Nayak, D. Paladino, N. D. Stockley, T. H. Johengen, A. W. Yu, S. Ruberg and A. Weidemann, Bioptical properties of Cyanobacteria blooms in western lake Erie, *Front. Mar. Sci.*, 2017, **4**(300), 1–20.
48 I. Gammoudi, N. Rokhaya Faye, F. Moroté, D. Moynet, C. Grauby-Heywang and T. Cohen-Bouhacina, Characterization of Silica Nanoparticles in Interaction with Escherichia coli Bacteria, *Int. J. Chem. Mol. Nucl. Mater. Metall. Eng.*, 2013, **7**(7), 520–526.
49 J. Van Heijenoort, Formation of the glycan chains in the synthesis of bacterial peptidoglycan, *Glycobiology*, 2001, **11**(3), 25R–36R.
50 Y. Luo, R. Zhao and J. B. Pendry, van der Waals interactions at the nanoscale: The effects of nonlocality, *Proc. Natl. Acad. Sci. U. S. A.*, 2014, **111**(52), 18422–18427.
51 C. Camilloni, D. Bonetti, A. Morrone, R. Giri, C. M. Dobson, M. Brunori, S. Gianni and M. Vendruscolo, Towards a structural biology of the hydrophobic effect in protein folding, *Sci. Rep.*, 2016, **6**, 28285.
52 G. Budin, H. Jung Chung, H. Lee and R. Weissleder, A Magnetic Gram Stain for Bacterial Detection, *Angew. Chem., Int. Ed.*, 2012, **51**, 7752–7755.
53 K. Jiang and P. Pinchuk, Temperature and size-dependent Hamaker constants for metal nanoparticles, *Nanotechnology*, 2016, **27**, 345710.
54 L. A. Wijenayaka, M. R. Ivanov, C. M. Cheatum and A. J. Haes, Improved Parametrization for Extended Derjaguin, Landau, Verwey, Overbeek Predictions of Functionalized Gold Nanosphere Stability, *J. Phys. Chem. C*, 2015, **119**, 10064–10075.
55 Y. Hu, N. Zhao, T. Gan, J. Duan, H. J. Yu, D. Meng, J. Liu and W. Liu, Analytic Method on Characteristic Parameters of Bacteria in Water by Multiwavelength Transmission Spectroscopy, *Hindawi J. Spectrosc.*, 2017, **2017**, 4039048.
56 T. S. Moore, C. B. Mouw, J. M. Sullivan, M. S. Twardowski, A. M. Burtner, A. B. Ciochetto, M. N. McFarland, A. R. Nayak, D. Paladino, N. D. Stockley, T. H. Johengen, A. W. Yu, S. Ruberg and A. Weideman, Bio-optical Properties of Cyanobacteria Blooms in Western Lake Erie, *Front. Mar. Sci.*, 2017, **4:300**, 1–20.
57 C. Salinas, M. V. Amé and A. G. Bracamonte, Synthetic non-classical luminescence generation by Enhanced Silica Nanophotonics based on Nano-Bio-FRET, *RSC Adv.*, 2020, **10**, 20620–20637.
58 K. Golberg, A. Elbaz, R. McNeil, A. Kushmaro, C. D. Geddes and R. S. Marks, Increased bioassay sensitivity of bioactive molecule discovery using metal-enhanced bioluminescence, *J. Nanopart. Res.*, 2014, **16**, 2770.
59 I. L. Medintz, A. R. Clapp, H. Mattoussi, E. R. Goldman, B. Fisher and J. M. Mauro, Self-assembled nanoscale biosensors based on quantum dot FRET donors, *Nat. Mater.*, 2003, **2**, 630–638.

60 S. Kaushal, S. S. Nanda, S. Samal and D. K. Yi, Strategies for the Development of Metallic-Nanoparticle-Based Label-Free Biosensors and Their Biomedical Applications, *ChemBioChem*, 2020, **21**(5), 576–600.
61 P. Lin, R. Owens, G. Tricot and C. S. Wilson, Flow Cytometric Immunophenotypic Analysis of 306 Cases of Multiple Myeloma, *Am. J. Clin. Pathol.*, 2004, **121**, 482–488.
62 C. Liu and C. E. Capjack, Effects of cellular fine structure on scattered light pattern, *IEEE Trans. Nanobioscience*, 2006, **5**(2), 76–82.
63 C. J. Van Oss, D. R. Absolom, A. W. Neumann and W. Zingg, Determination of the surface tension of proteins I. Surface tension of native serum proteins in aqueous media, *Biochim. Biophys. Acta, Protein Struct.*, 1981, **670**(1), 64–73.
64 A. G. Bracamonte and A. V. Veglia, Spectrofluorimetric determination of Serotonin and 5-hydroxyindoleacetic acid in urine with different cyclodextrin media, *Talanta*, 2011, **83**, 1006–1013.
65 M. L. Wilson and L. Gaido, Laboratory Diagnosis of Urinary Tract Infections in Adult Patients, *Med. Microbiol.*, 2004, **38**, 1150–1158.
66 V. Benigno, S. D. Peri, A. Bianco, R. Cusimano, F. Varia, G. Ziino, M. C. Failla and D. Natoli, Quantitative determination of urine bacteria in the diagnosis of urinary tract infections in children, *Minerva Pediatr.*, 1990, **42**(4), 143–146.
67 N. L. Pacioni and A. V. Veglia, Determination of carbaryl and carbofuran in fruits and tap water by β-cyclodextrin enhanced fluorimetric method, *Anal. Chim. Acta*, 2003, **488**(2), 193–202.
68 M. Nemati, Al. Hamidi, S. Maleki Dizaj, V. Javaherzadeh and F. Lotfipour, An Overview on Novel Microbial Determination Methods in Pharmaceutical and Food Quality Control, *Adv. Pharm. Bull.*, 2016, **6**(3), 301–308.
69 R. Zhou, X. Zhang, Z. Bi, Z. Zong, J. Niu, Y. Song, D. Liu and S. Yanga, Inactivation of Escherichia coli Cells in Aqueous Solution by Atmospheric-Pressure N2, He, Air, and O2 Microplasmas, *Appl. Environ. Microbiol.*, 2015, **81**(15), 5255–5265.
70 S.-O. Shan and D. Herschlag, The change in hydrogen bond strength accompanying charge rearrangement: Implications for enzymatic catalysis, *Proc. Natl. Acad. Sci. U. S. A.*, 1996, **93**(25), 14474–14479.
71 J. Miller and J. Miller, *Statistics and Chemometrics for Analytical Chemistry*, Prentice Hall, 4th edn, 2001.
72 N. S. Barteneva, E. Fasler-Kan and I. A. Vorobjev, Imaging Flow Cytometry: Coping with Heterogeneity in Biological Systems, *J. Histochem. Cytochem.*, 2012, **60**(10), 723–733.
73 D. Brouard, O. Ratelle, A. G. Bracamonte, M. St-Louis and D. Boudreau, Direct molecular detection of SRY gene from unamplified genomic DNA by metal-enhanced fluorescence and FRET, *Anal. Methods*, 2013, **5**, 6896–6899.
74 J. N. Miller and J. C. Miller, *Statistics and Chemometrics for Analytical Chemistry*, Pearson Education Canada, 6th edn, 2010, ISBN-13: 978-0273730422.
75 C. Salinas and A. G. Bracamonte, From Microfluidics to Nanofluidics and signal Wave-guiding for Nanophotonics, Biophotonics resolution and Drug Delivery, *Front. Drug Chem. Clin. Res.*, 2019, **2**, 1–6.
76 C. Salinas and G. Bracamonte, Design of Advanced Smart Ultraluminescent Multifunctional Nanoplatforms for Biophotonics and Nanomedicine applications, *Front. Drug Chem. Clin. Res.*, 2018, **1**(1), 1–8.
77 G. T. Hermanson, *Bioconjugate Techniques*, Elsevier, 2nd edn, 2008.